UCLouvain

École polytechnique de Louvain

Optimization of Nanostructured Organic Cathode Li_4-*p*-DOBDA

Authors : **Endy Nugroho DWIPUTRA**
Supervisors : **Prof. Alexandru VLAD**
Readers : **Prof. Joris PROOST**, **Prof. Yaroslav FILINCHUK**
Academic year 2022–2023
Master in Chemical and Materials Engineering

Acknowledgments

First and foremost, I would like to express my heartfelt gratitude to my Lord for granting me this wonderful opportunity. I am also immensely grateful to every people who have directly or indirectly contributed towards the completion of my Master's thesis and elaboration of this manuscript.

I am deeply thankful to Prof. Alexandru Vlad for allowing me to be a part of this research group at IMCN and for providing me the opportunity to conduct my Master's thesis in his laboratory. Over the past 9 months, this experience has expanded my horizon towards organic battery research, broadened my perspective and opened up opportunities for further research in the energy storage field. I am truly appreciative of your support, guidance and knowledge for both my Master's thesis and my Ph.D. applications. Thank you for inspiring me toward the next big step in my research career.

I would like to acknowledge the invaluable support and mentorship of Dr. Rambabu Darsi. Your patience and guidance have been instrumental in my growth as a researcher, especially as I started with limited exposure to organic research. Your insightful feedback, a thorough review of my thesis, as well as encouraging support and guidance toward the right direction in my scientific approach and preparing for Ph.D. life, have been truly invaluable. I am also grateful for the assistance of Dr. Bakuru Vasudeva in testing and collecting XRD data, Dr. Shubhadeep Pal in SEM data collection and analysis, as well as cell-making and testing, Dr. Petru Apostol in preparing organic synthesis, Dr. Binson Babu in providing helpful insights, Da Tie in troubleshooting battery testing software, Fabio Lucaccioni in lab troubleshooting and supplying lab materials, Dr. Andrii Kachmar for technical support in lab work, Robert Markowski for answering initial queries that bring my decision in Master thesis here, as well as valuable suggestions in thesis presentation and Q&A session, along with Geraldine's insights too.

I would like to express my gratitude to every NRJ group member who has contributed no matter how small, to my research and lab work. I will miss the friendly gestures from Jerome and Tom, for their friendship that boosts my morale during the busy final year of my Master's. I will genuinely miss Dr. Gulshan Kumar for his wise insights and enlightening experience in the research world, as well as for being a trusted confidant during challenging times, which I really sincerely appreciate and grateful for.

I am thankful to the FAME Erasmus Mundus Master Program, for all the coordinators and representatives, (especially Dr. Joachim Broetz in TUD and Dr. Benoit Hackens in UCL), in which my admission has been both a miracle and a dream come true, providing me with an exceptional education and invaluable experience. I am also thankful to my friends and family's support, especially my mother who has always believed in me, and provides unwavering support, in giving me love and strength to persevere despite challenging times when I was doubtful, lost my way and questioned myself. This thesis would not have been possible without all of your support. Thank you once again from the bottom of my heart.

Abstract

Renewable energy and electric vehicles (EVs) play a crucial role in achieving EU's 2050 goals. Consequently, there is a growing demand for robust energy storage systems. While Lithium-Ion Batteries (LIB) have emerged as a most promising solution due to high energy density and relatively lower energy cost per unit, the exponential surge in demand for Lithium (Li) raises concerns about potential resource depletion, as reserves of Li supplies are not unlimited. Alternative solutions are being explored, particularly those that are abundant, similar, sustainable, safe, cost-effective and can be derived from renewable sources. Organic batteries have garnered significant research interest and momentum in recent years, meeting many of these criteria while offering comparable electrochemical performance that potentially will catch up with commercial LIBs in the future.

Among the various organic molecules being considered, an air-stable Li_4-*p*-DOBDA cathode stands out as a viable and attractive option. Synthesized under an inert atmosphere using the Schlenk tube method, this cathode exhibits two-electron redox processes, with an average redox potential of 3.35 V vs. Li^+/Li comparable to the commercial Lithium Iron Phosphate (LFP) battery, while having a high theoretical specific capacity of 214.51 mAh/g. The material properties of Li_4-p-DOBDA are also evaluated using characterization techniques such as FTIR, SEM and XRD.

However, challenges exist that hinder its implementation on a larger scale. Issues related to polarization and solubility lead to rapid capacity fading as the active material gets dissolved during cycling. To mitigate these challenges, the particle size of the cathode material is reduced through ball-milling, resulting in particles ranging from hundreds of nm to 1 μm. This particle size reduction increases the contact surface area of the electrode composite, thereby reducing polarization and solubility. Notably, this approach yields improved electrochemical performance, particularly when used in conjunction with 10%Graphene-SP at a frequency of 25 Hz (G-SP 25 Hz).

Finally, the potential of the organic cathode extends beyond LIBs, as it is transferrable to the post-LIB system. A preliminary assessment of the material properties and electrochemical performance is conducted for Na_4-*p*-DOBDA, providing insights into the redox phenomena, in comparison with Li_4-*p*-DOBDA, as well as facilitating further investigation of its chemistry and optimization as a viable alternative solution.

List of Abbreviations

A	Ampere
Al	Aluminum
BQ	Benzoquinone
C	Carbon
Ca	Calcium
Cl	Chlorine
Co	Cobalt
CN	Nitrile
CP	Coordination Polymer
CSA	Conjugated Sulfonamide
C_{th}	Theoretical Capacity
CV	Cyclic Voltammetry
DHTPA	2,5-dihydroxyterephthalic acid
DOL	1,3-Dioxolane
DMC	Dimethyl Carbonate
DME	Dimethoxyethane
DFT	Density Functional Theory
EC	Ethylene Carbonate
ED	Energy Density
EDG	Electron-donating group
EWG	Electron-withdrawing group
EVs	Electric Vehicles
F	Fluorine

Fc	Ferrocene
Fe	Iron
Fig.	Figure
FTIR	Fourier-Transform Infrared Spectroscopy
FWHM	Full Width at Half Maximum
GCD	Galvanostatic Charge-Discharge
h	hour(s)
H_4-p-DOBDA	2,5-Dihydroxy-1,4-benzenediacetic acid
HOMO	Highest unoccupied molecular orbital
HQ	Hydroquinone
K	Potassium
KB	Ketjenblack
LCO	Lithium Cobalt Oxide
LFP	Lithium Iron Phosphate
Li	Lithium
LMNO	Lithium Manganese Nickel Oxide
Li_4-*p*-DOBDA	tetralithium 2,5-dihydroxy-1,4-benzenediacetate
LIB	Lithium-ion battery
LUMO	Lowest unoccupied molecular orbital
M	Metal
Mg	Magnesium
Mn	Manganese
MOF	Metal-organic Framework
Na	Sodium
Ni	Nickel

NMR	Nuclear Magnetic Resonance
NS	Normal-sonicated
OBs	Organic Batteries
OBM	Organic Battery Material
ONEM	Organic Negative Electrode Material
OPEM	Organic Positive Electrode Material
PC	Propylene carbonate
PTFE	Polytetrafluoroethylene
PTtSA	Benzene-1,2,4,5-tetrayltetrakis((methylsulfonyl)amide)
PS	Probe-sonicated
PXRD	Powder X-ray diffraction
R&D	Research & Development
RT	Room temperature
SEI	Solid electrolyte interphase
SHE	Standard hydrogen electrode
SIB	Sodium-ion battery
SP	Super P
t	ton
TEM	Transmission Electron Microscopy
TFSI	Bis(trifluoromethane)sulfonimide
TM	Transition metal
V	Volt
W	Watt
Zn	Zinc

Table of Contents

List of Figures

List of Tables

I. Introduction

I.1 General Context on Energy Storage

The world's population, which is rapidly approaching 8 billion people, is witnessing a significant increase in energy demand due to population growth and technological advancements in the energy sector [1]. This situation necessitates higher energy consumption, primarily relying on conventional energy sources such as oil and gas, which currently account for approximately 80% of the global energy supply [2]. However, the limited availability of resources and potential depletion in regions with high demand can lead to geopolitical conflicts, as exemplified by the ongoing Russia-Ukraine war. Furthermore, the escalating emissions of greenhouse gas, particularly CO_2, have resulted in global warming with emissions increasing by 75% in the past 35 years. Addressing these issues is crucial for sustainable living on Earth.

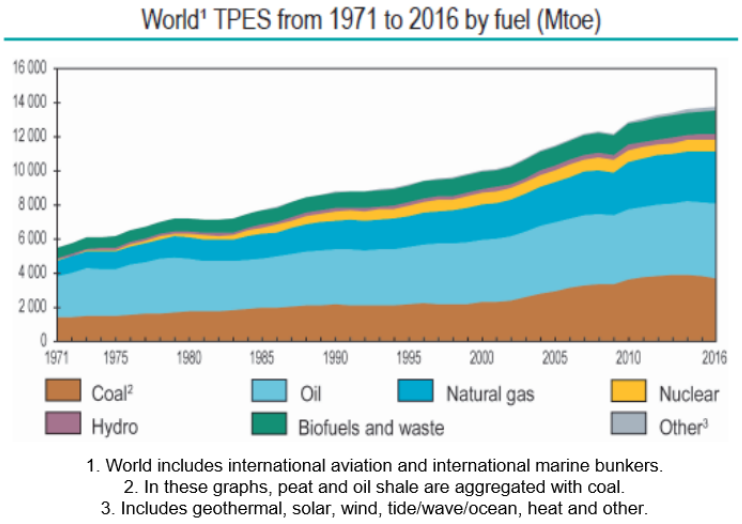

Figure 1 Electricity Generation from Various Non-Renewable and Renewable Sources in the World

In the light of increasing environmental concerns and the projected growth in energy consumption, achieving sustainability becomes a crucial focus, especially in energy production. Lithium mining has intensified to meet the surge of demand in various essential applications such as electronics, renewables and EVs in order to meet the rapidly escalating energy requirements. It is anticipated that the global rate of energy production needs to be doubled by 2050 to meet the world's energy demand requirement [3].

To address the urgent challenge of reducing carbon emissions and achieving carbon neutrality by 2050, the European Union (EU) and numerous other countries have committed to minimizing their

environmental impact. Cleaner energy production can be achieved through the utilization of renewable energy sources, which are not only abundant, but also have a lesser ecological footprint [4]. Despite increasing progress, the EU's current reliance on renewables stands at approximately 21.8% (including solar, wind, water, biomass and other sources), as indicated in figure 2, which is far from ideal pace in meeting the EU's 2050 goals [5].

Nonetheless, the intermittent nature of renewable energy poses an ongoing challenge for its widespread adoption and daily usage due to inherent variations in supply and demand. The timing of peak energy production and demand are unlikely to coincide [6]. For instance, solar energy exhibits its highest output during mid-day, whereas peak demand typically occurs in the early morning and evening hours. Moreover, the conversion efficiency of renewable energy into usable energy remains considerably lower compared to conventional fossil fuel sources such as oil and gas. Consequently, substantial research & development (R&D) efforts are being dedicated to improving renewable technologies to address this imminent threat.

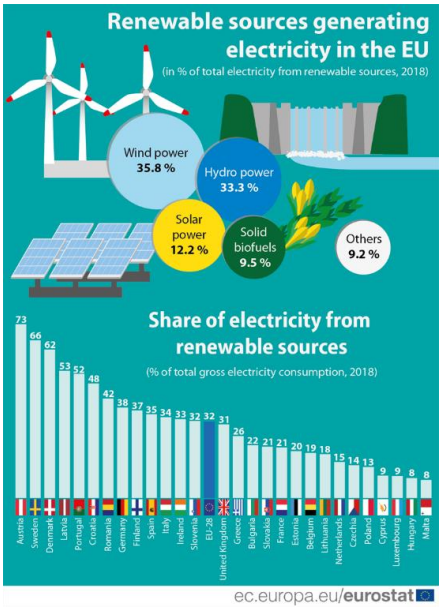

Figure 2 Electric energy proportion in EU coming from Renewable Energy Sources [6]

Overcoming these challenges can be achieved through the implementation of energy storage systems, enabling consumers to utilize the generated energy at any time by normalizing and storing it for the peak consumption period [7]. While the development of a smart energy grid isa driving force for improving energy storage systems, the urgency to transition to electric vehicles (EVs) by 2035 and establish the necessary infrastructure further motivates advancements in electrochemical energy

storage systems (EES). EES is crucial for the reversible storage of electrical energy in the form of chemical energy, which is essential for this transition in supporting widespread adoption of EVs [8].

The first EES system was discovered by Alessandro Volta in 1800, which involved redox reactions between copper (Cu) and Zinc (Zn), and the energy produced was primarily determined by the difference between their redox potential [9]. The batteries then evolved from primary to secondary battery, as Lead-acid battery being developed as a widely used automotive industry solution. This battery utilized a Sulfuric acid electrolyte, which offers a low energy density (ED) of 55 Wh/kg and a nominal voltage of 2.05 V [10]. Subsequently, Nickel-Cadmium (Ni-Cd) batteries were introduced, but was replaced by safer and non-toxic Nickel-Metal Hydride (Ni-MH) batteries. Ni-MH batteries exhibit ED ranging between 40 to 80 Wh/kg, with nominal voltage of 1.2 V for lifespan up to 2000 cycles [11]. However, these technologies are susceptible to the memory effect, resulting in gradual capacity loss due to repeated incomplete charging and discharging.

The significant breakthrough came with the extensive development of Li-ion batteries (LIB), which was derived from Li metal primary batteries (LMB) between 1970s-1980s. LIBs were ultimately commercialized by Sony and Asahi Kasei in 1991 [12]. LIB outperforms its predecessor technologies, in terms of voltage and gravimetric energy density, which reaches the voltage of 3.6-3.7 V and more than 200 Wh/kg, respectively [13]. The superiority of LIBs can be attributed to the very light element of Li, with a molar mass of approximately 6.941 g/mol. This characteristic enhances the specific energy and capacity, reaching around 3860 Ah/kg, coupled with very low redox potential of -3.045 V vs. Standard Hydrogen Electrode (SHE) against Li^+/Li couple. This high Capacity and Voltage difference contribute to LIBs' high specific energy, leading to their rapid market growth with billions of cells sold annually since their commercialization debut. This growth is evident in the Ragone Plot depicted in figure 3 [14].

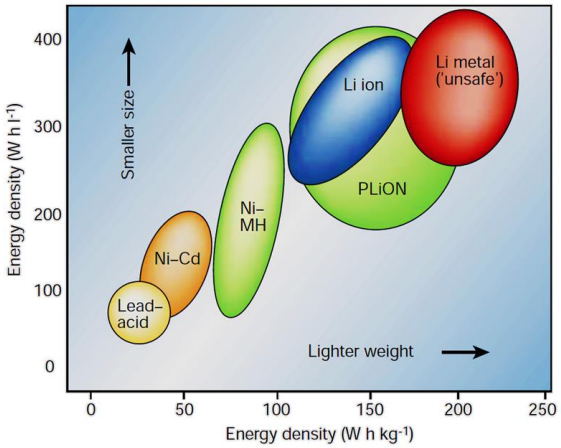

Fig. 3: Energy Density Evolution with Battery Technology Development [14]

I.2 Working principles of Lithium-Ion Battery

As illustrated by the diagram in figure 4, LIB components can be divided into negative (anode) and positive electrode (cathode), which is separated by a porous membrane (separator), that has been soaked with a liquid electrolyte, in this case it contains a suitable organic solvent with Li salt. The working principle, which is called rocking-chair mechanism, wherein Li^+ ions diffuse reversibly between both electrodes in parallel while electrons transfer through the external circuit. During discharging, oxidation occurs at the anode, where Li^+ ions are liberated towards the cathode [15]. The initial electrochemical potential gradient, with low (negative) and high (positive) potential gradually dissipates until the system reaches equilibrium potential. The charging progress happens in reverse direction of what was described above, from cathode towards anode instead.

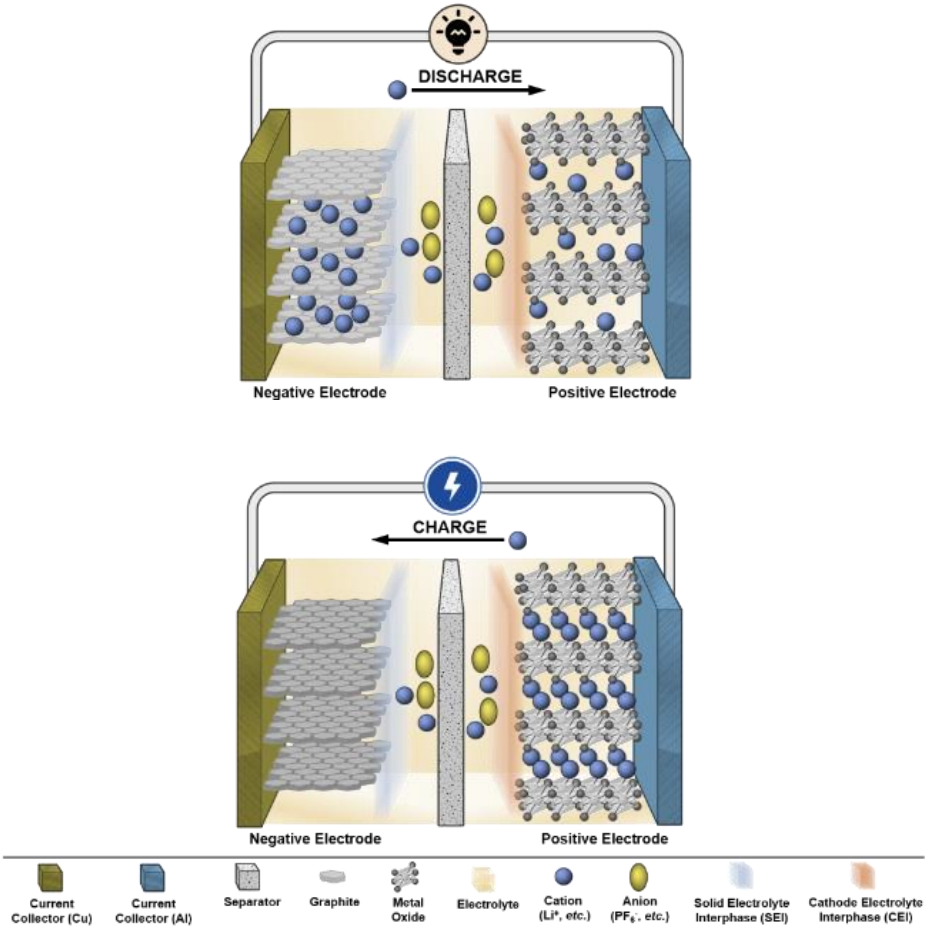

Fig.4. A schematic of the working principles illustrated by LCO in LIB. Lithium ions diffuse from a lithiated graphite (Li_xC_6) anode during discharge into delithiated $Li_{1-x}CoO_2$ cathode. The reverse process occurs during charging [15].

Various classes of materials that have been developed as electrodes in LIB. In the case of cathodes, layered material such as LCO ($LiCoO_2$), spinel material LNMO ($LiNi_{0.5}Mn_{1.5}O_4$), ternary cathode NMC ($LiNi_{1/3}Mn_{1/3}Co_{1/3}O_2$), and olivine material such as LFP ($LiFePO_4$) are the most commonly used in commercial batteries nowadays. The advantages of LCO and NMC lie on their high energy density, while LFP has good chemical & thermal stability, fast charging capability, low self-discharge rate, longer lifespan, wider operating temperature range and improved safety [16]. Next generation inorganic compounds, such as LNMO, are being considered for practical applications, due to its high voltage of 5V and being Cobalt-free, which reduces cost, environmental concerns and criticality issues. However, further improvements are needed to enhance the cycling stability of LNMO, especially at higher potentials [17].

Regarding anodes, graphite is the most frequently used material. Graphite exhibits high capacity, excellent stability and the lowest potential possible close to 0V vs. Li/Li^+, contributing to its overall good performance. Another anode that had been explored in earlier studies is the Li metal anode, which offers high capacity (10 times greater than graphite) and operates at very low potential (-3.04V vs. SHE). Despite these factors, the use of Li metal anodes upon cycling presents challenges such as dendrite growth and formation of "dead" Li. Dendrites can grow from one end of the electrode to another, leading to short-circuits, safety concerns and efficiency losses. Ongoing research aims to overcome these pitfalls associated with Li metal anode [18].

During the operation of LIB, various chemical reactions occur at the interface between the electrolyte and electrode. Specifically, the electrolyte at the anode undergoes decomposition, which is dependent on its composition and stability window, leading to the formation of Solid Electrolyte Interphase (SEI), on the surface of the anode, which significantly impacts the overall performance of the battery. The SEI is formed after the first cycle, which leads to reduction in subsequent capacity and increased polarization between charge and discharge cycles. Optimizing the SEI is crucial, as it is desirable for the SEI to be electronically insulating to block the flow of electrons, while remaining ionically conductive to allow diffusion of ions. Additionally, the SEI should exhibit chemical and mechanical stability to ensure long-term performance and reliability [21]. Moreover, SEI is also shown to be dynamic layer, in which its formation in terms of thickness and composition will vary upon cycling. The interplay between the SEI, electrode materials and electrolyte in LIB system remains a complex system that requires further parallel studies to better understand and enhance LIB performance, particularly for large-scale applications in renewables, stationary system or mainly EVs, considering the imminence and urgency of achieving EU 2050 goals [4].

I.2.1 Lithium-Ion Battery Performance

Battery functions to deliver a certain amount of energy to power a device. Before delving into the specific chemistries of different organic redox compounds, it is important to consider several key parameters when designing new electrode materials and understanding their electrochemical properties.

The performance metrics is often described by using the specific (Wh/kg) and volumetric (Wh/m^3) energy density (ED), which represents energy stored in an hour per kg or per material's unit volume, respectively. The specific ED is derived from the specific capacity (Ah/kg), which is the amount of charge a battery can deliver per unit mass, multiplied by the voltage (V), which is the potential difference between both electrodes.

The amount of energy that battery provide can be increased by tuning the specific capacity and voltage, which values are obtained from galvanostatic measurement, *i.e.*, by applying constant current in a series of charge-discharge cycles. High capacity can be achieved when both electrodes have low molecular mass and can facilitate multiple electrons transfer redox reactions. The theoretical gravimetric capacity ($\underline{Q_T}$), defines the maximum or theoretical amount of electricity that can be delivered per unit mass when the active electrode is completely discharged; which is calculated as follows:

$$Q_T = \frac{nF}{3600M}\ (Ah\ kg^{-1}\ or\ mAh\ g^{-1}) \ldots (1)$$

In the formula provided, *n* is identified as the number of exchanged electrons, F refers to the Faraday constant (96500 C mol^{-1}) and M denotes the molar mass of the active material (kg mol^{-1}). Optimizing the theoretical capacity Q_T involves maximizing the ratio of n/M.

Similarly, high voltage can be gained not only by potential difference but also exhibiting redox process at the highest and lowest potential. The redox potential signifies the potential at which an electrochemical reaction (redox) occurs. This intrinsic parameter is influenced by the electroactive material and its electronic environment, which impact the energy levels of molecular orbitals. Consequently, this determines the ionization energy and electron affinity of the molecule [19]. This makes Li metal, which exhibits the lowest redox potential and possesses low molecular mass, resulting in its high capacity and overall high energy density [20]. When considering the Capacitance-Voltage

curve, optimizing the potential window becomes critical for maximizing energy density, without sacrificing long-term cycleability due to solubility issue.

Cycling stability is another important parameter in batteries, as ideally battery should behave like a “rocking chair”, which is able to retain their charge without any significant loss of charge after each cycle. This property is described by capacity retention and Coulombic efficiency, which represents the ratio between the injected and extracted capacity in a full cycle during cycling. Achieving good cycling stability relies on the reversibility of the redox reaction, meaning the electrochemical reaction must be chemically and thermodynamically stable in both directions, during charging and discharging. In the cycling stability curve, this is quantified by its Coulombic or Faradaic efficiency for chemical reversibility, while voltage efficiency pertains to thermodynamic reversibility. Good cycling stability, such as that observed in commonly used graphite electrodes, is characterized by minimal loss of specific capacity during charge-discharge cycles [14]. For instance, the LCO cathode is currently limited to be stable up to a working potential of 4.5V and ongoing R&D aims to extend this potential range while maintaining good cycling stability for achieving higher energy density.

Another important parameter is cycle lifetime, which represents the total number of charge-discharge cycles a battery undergo before its capacity diminishes to a certain percentage of its initial reversible capacity. This parameter is determined by complex interaction between electrode and electrolyte during the cycling process. Capacity loss or fading is particularly pronounced in organic batteries, as organic materials tend to exhibit solubility issues caused by the electrolytes during cycling, leading to the loss of active materials and capacity. Addressing this issue involves the addition of high surface area carbons as a “sponge” to reduce the elution of active materials while enhancing the conductivity. Nonetheless, this approach increases the inactive mass, resulting in a lower energy density, as a trade-off [21].

Furthermore, the C-rate, which measures the rate at which a battery is being charged or discharged, quantified by the value of current density (mA g^{-1}) that is normalized over its theoretical current density that can be delivered in 1 hour. In addition, it is essential to consider other factors such as cost, complexity, and environmental impact throughout the battery’s entire life cycle. Ideally, the battery manufacturing process should be cost-competitive, utilize minimal to no toxic elements and rely on abundant resources. Since the focus of the master thesis is on cathode materials, further discussion will revolve around this topic.

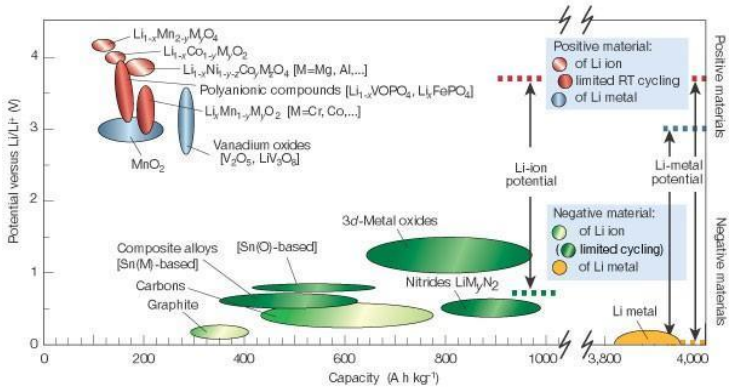

Figure 5 Comparison of the working potential vs. specific capacity between different cathode and anode systems [14].

Moreover, safety is of utmost importance in battery to prevent accidents such as thermal runaway and self-ignition (when in contact with oxygen), which can lead to fires and explosions. A notable example is the recall of 2.5 million units Galaxy Note 7 phones [22]. Proper heat dissipation is crucial to remove the generated heat and ensure that the battery's temperature does not exceed its operating range. Safety considerations encompass the properties of the active materials, electrolyte and overall battery design, which can be adjusted by incorporating small addition of additives to improve its thermal stability. In commercial applications, LFP batteries are predominantly used due to its excellent safety profile, despite having lower specific capacity and cycling stability compared to [23]. Finally, sustainability factor plays a significant role in the development of new battery materials, especially in achieving the EU2050 carbon neutrality goal, which aims to minimize the environmental impact as much as possible [24].

I.2.2 Sustainability Issues of Current Battery Materials

LIB is the most prevalent among domestic and personal usage as its demand has been exponentially rising that projected to rise from 526 GWh in 2020 to 9300 GWh by 2030 due to its high energy density ranging between 260-270 Wh/kg [8], [9]. However, the critical issue lies in the increasingly scarcer Li abundance in the Earth's crust, comprising only 0.002 – 0.006 %. With the anticipated continuous growth in demand, particularly in e-mobility systems, hence alternative materials with comparable performance are being investigated as potential alternatives [25]. Currently, Li poses challenges in terms of disposal, as it is highly flammable upon contact with water or oxygen, on top of not all Li is can be effectively recycled. This limitation further depletes Li supplies when demands increase

exponentially [25]. Furthermore, the widespread use of commercial LIB also relies heavily on the extraction of other metals such as Cobalt (Co), predominantly sourced from regions such as Congo, China, Australia and South America. This non-uniform geographical concentration of deposits poses significant concerns with exponentially higher demands of LIB, and will not be sustainable over longer term as it depends on reliable supply of critical metals [26].

I.3 Future of Li

The increasing production of renewable energy is expected to lead to a rise in LIB production. However, this growth faces a significant challenge due to the limited supply of Li, which may become depleted and will not be sufficient to meet the future energy demand necessary for realizing a carbon-neutral future. Despite Li being the 33rd most abundant element in the Earth's crust, current estimation suggests that there are only 89 million metric tons (Mt) of Li reserves available, with only 22 Mt being economically recoverable at present. Additionally, the surging demand for Li resulting from the widespread adoption of EVs raises concerns about the longevity of Li supplies. According to United States Geological survey, these supplies may only last for the next 10-20 years [27].

While recycling Li offers a potential solution to prolong the usability of available Li, it is worth noting that in 2019, only 9% of the Li demand could be satisfied through recycling efforts. Consequently, the search for alternatives to Li has become increasingly urgent in order to circumvent the looming supply shortage in the coming decades while simultaneously fulfilling the performance and ecological footprint criteria. In that case, Ni-Cd or Lead-acid batteries are deemed unsuitable due to its toxicity and other environmental issues when compared to LIBs.

In addition to Li, other rare or scarce elements found in LIB as well, such as Cobalt (Co), pose sustainability concerns in the long term. Co is principally used in LCO and NMC cathodes. The global Co reserves are estimated to be around 7 Mt, with 60% of the reserves are located in Democratic Republic of Congo. Apart from sustainability issues, the reliance on Co presents criticality, ethical, political and economic challenges, as Co is obtained through the exploitation of children under improper conditions, as well as with escalating price due to an almost monopolistic approach [27].

Since the commercial introduction of LIBs, they have predominantly consisted of metal-based cathodes, which are inorganic compounds. These cathode materials fulfil key requirements such as reduced phase which contains Li-ion, stability in ambient air and ease of battery processing. However, as some of these inorganic compounds usually contain rare and/or toxic elements, requiring energy-intensive ceramic treatments during industrial production. Therefore, exploring alternative materials

for a sustainable future becomes crucial, considering their minimal environmental impact in terms of carbon and energy footprint, as well as reduced scaled-up cost [28]. Various classes of materials are being investigated and discovered for their feasibility in future batteries.

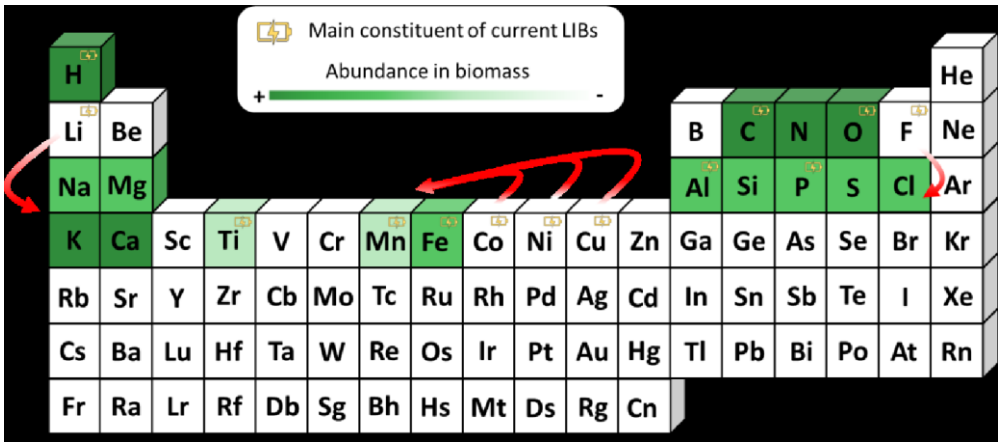

Figure 6 Mismatch between elements and main constituents constituting biomass and of present LIBs, adapted from [28].

Given the disparity between demand and resources, and considering other factors for future sustainability, it is essential for new technologies to consider alternative materials for a greener future. These materials include more abundant elements such as sodium (Na), calcium (Ca), iron (Fe), manganese (Mn), potassium (K), magnesium (Mg), and carbon (C) (Fig. 6). Addressing the criticality and sustainability issues involved in Li and Co sourcing can be achieved through exploration of post-Li battery technologies and the utilization of organic electroactive materials [28].

I.4 post-Li Technologies

Based on the preceding discussion, the development of alternatives to Li-based battery technology is necessary. These alternatives should utilize more abundant elements (such as Na, K, Mg, Ca or Zn) while providing similar or higher specific energy densities. Sodium-ion batteries (SIB) have gained attention due to the increasing availability of Na's abundance, which is commonly found in kitchen salt [29]. However, SIB face certain limitations due to its unique chemistry. Their potential anode materials are currently restricted to hard carbon, as SIBs employ a 3D insertion mechanism instead of the 2D intercalation mechanism used in LIBs. This limitation hampers the practical application of SIBs. Furthermore, SIBs exhibit poor stability in the formation of a solid electrolyte interphase (SEI) during

cycling, resulting in a decreased practical energy density and electrochemical performance compared to LIBs, which decreases further, for its performance to compete compared with LIBs.

Divalent elements such as Mg and Ca possess significantly higher abundances in the Earth's crust that are 1000 to 10000 greater than that of Li. They also offer high volumetric capacity and exhibit smoother electrodeposition behaviour. However, these advantages come with certain challenges. Firstly, there is a compatibility issue between the electrolyte anions and the metal. When conventional Li-salts' anions, such as PF_6^- and ClO_4^- react with the metal, leading to the formation of a passivating layer. This layer blocks further transport of Mg^{2+} or Ca^{2+} ions which prevents reversible plating/stripping at the electrode interface. The second challenge arises from the difficulties in solvation separation. The small size of the cations, coupled with its divalent charge, result in high Coulombic attraction. This high charge density requires significantly high energy to separate interactions between the cation and solvent molecules during transport to the opposite electrode and subsequent de-solvation at the interface [30]. This poses a considerable obstacle in finding suitable electrolytes that allow for reversible cycling and long-term stability, as this issue undermines the purpose of a rechargeable battery. Hence, other alternatives need to be investigated, including organic molecules that employ different mechanisms and warrant further investigation and discussion.

II. Literature Review

II.1 Organic Batteries

Among the various alternative energy storage systems, organic batteries (OB) emerge as an enticing solution when compared to commercially available inorganic energy storage systems. OBs offer several advantages, including reduced demand for critical and rare earth metals, less environmental footprint in both production and recycling, resulting in more cost-effective manufacturing scalability by eliminating hefty extraction processes. Although OBs currently have not provided competitive volumetric energy density compared to the current inorganic system, they possess a natural abundance of organic molecules (C, H, O, N and S) that can be easily sourced from biomasses using green chemistry processes.

Furthermore, OBs also demonstrate high flexibility in terms of molecular diversity and structural designability. By exchanging substituent functional groups, the redox voltage and other thermodynamic and electrochemical properties (such as stability, reduced solubility and molecular weight) can be fine-tuned. This vast variety enables the use of organics as both cathode and anode materials, making OBs into an all-organic battery. Additionally, OBs also significantly greener by reducing carbon and energy footprint, making them a fantastic solution that potentially has high gravimetric energy density in the future, especially when scaled up [31]. Furthermore, the OB system can be further developed and extended towards post-Li ion batteries, including Na, K, Mg, Ca and Zn batteries [32].

When optimized, OBs can possibly achieve charge/discharge with very high rates (up to 120 C), which failure is inevitable for current intercalation compounds at that rapid rate [33]. The molecular flexibility of OBs allows for more than one electron exchange during redox processes, enhancing their discharge and charge capabilities [34]. In addition, OBs also tend to be non-flammable and non-toxic, simplifying its disposal procedures [35]. Thus, OBs have experienced significant advancements in recent years, especially on the investigation of its redox chemistries and suitable electroactive compounds.

Historically, initial investigations on organic materials as components for battery electrodes originated in the 1960s. In 1969, soluble dicholoroisocyanuric acid was used as an active cathode material for the Li-organic Dry Tape Battery, which yields a potential of 3.1 V *vs.* Li^+/Li and efficiency between 60-70% [36]. The exploration was continued further until late 1990s, especially on doped conjugated polymers (CPs), such as polyaniline and polythiophene [37]. Even though CP-based Li-metal batteries displayed energy density and cycling stability comparable to lead-acid batteries, however the safety risks posed

by unsafe Li anode and organic electrolytes led to a decline in research on organics. During this period, emphasis shifted to inorganic intercalation compounds, which offered higher energy densities, high voltage potential, simpler synthesis steps that eliminates the solvent requirement, as well as lower conductive carbon additives are required.

Nevertheless, research on other organic compounds, such as organosulfurs and radical polymers was progressing in the background [38, 39]. Due to environmental and energy concerns, the interest towards organic battery electrodes was reignited in the late 2000s, as carbonyl compounds were reported to provide high gravimetric energy density and sufficient cycling stability [40]. With progressive organics' research in molecular design strategies, achievable battery performances and the potential for reduced environmental impact, organic redox compounds holds substantial promise to be viable as future sustainable battery systems [41].

OBs are regarded as a promising future alternative battery systems, especially for stationary domestic applications that do not require high energy density, as well as in electric vehicles or other mobile applications, but prioritizing sustainability aspect [42]. Additionally, OBs benefit from abundant raw materials at a significantly lower cost compared to Li [43]. While OBs currently have lower energy and power density than inorganic LIBs, they demonstrate promising potential [44]. Once the organic cathode can reach a potential more than 2.91 V vs. Li^+/Li, which is equivalent to Oxygen reduction potential, then it also becomes stable under ambient air condition.

On the other hand, before OBs can be commercialized and reach the level of prevalence seen in LIBs today, still has extensive R&D are required. Firstly, it is a poor electrical conductor, which limits its capacity and long-term capacity. To address this issue, additional conducting substances such as Carbon are necessary, which adds inactive material mass, and in turn reduces its volumetric and gravimetric capacity. Similarly, with other organic or smaller molecules, it can easily become soluble as dissolution in electrolytes is common issue for this class [34]. Nonetheless, turning it into polymers will decrease solubility, but it comes with a trade-off in lower capacity. Finally, organic molecules due to its lower density and less compact molecular architecture will occupy more volume than its inorganic counterparts, hence it will also lower volumetric capacity and energy density. Further research is needed to address and optimize these issues for the future viability of OBs as efficient and reliable energy storage systems.

II.2. Organic Redox Mechanism and Overview of Organic Battery Materials

In the realm of organic electrode materials, there are three families of Organic Battery Materials (OBM) categorized based on their redox system, which are classified as p-type, n-type or b-type (figure 7) [45]. P-type molecule (e.g., conjugated amines) forms a positively charged species upon reversible oxidation of a neutral molecule. Conversely, n-type molecule (e.g., quinones) forms a negatively charged species upon reversible reduction process. In p-type, the process is accompanied by the release of a redox inactive anion (such as PF_6^-, $TFSI^-$, BF_4^-, ClO_4^-, …) to balance the generated positive charge. Similarly, in n-type a redox inactive cation (such as H^+, Li^+, Na^+, K^+, Mg^{2+}) is released upon oxidation to compensate for the negative charge. P-type materials reveal high redox potential (>3V vs. Li/Li^+), however they suffer from lower specific capacity than n-type because of the higher molecular weight from both redox active materials and stored anions. In n-type materials, it exhibits a wider operating redox potential window (between 1-3.5 V vs. Li^+/Li) that allows this class to be used as both cathodes and anodes. Moreover, organic molecular crystals demonstrate greater tolerance towards structural changes, which makes this system adaptable for post-Li technologies involving Na, K, Mg or Ca. Lastly, a bipolar or b-type materials (e.g. nitroxide radicals) can flexibly switch to become negative upon reduction (n-type mechanism) or to positive upon oxidation (p-type mechanism). The inactive ions exchanged are present in the electrolyte used (such as $LiPF_6$ salt), which ensures the ionic conduction between electrodes.

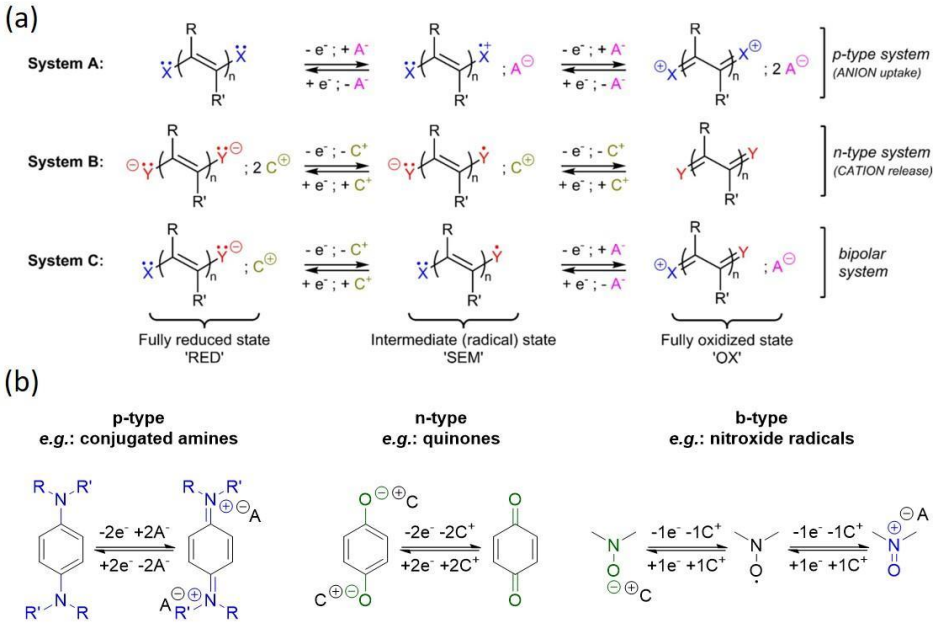

Figure 7 (a) The three redox mechanisms available in organic active compounds [49]. (b.) Examples of chemistry for each proposed mechanism

As the boundary between cathodes and anodes are blurry, the literature suggests that a redox process below 2V *vs.* M^{x+}/M is generally considered as anodic materials, while a redox process above 2V *vs.* M^{x+}/M as cathodic material based on the reported data.

II.2.1 Organic Electrode Materials

Ideal Cathode materials for organic batteries should have high redox potential with a wide range of operating voltage, with high specific capacity, good chemical stability with the electrolyte, as well as good ionic and electronic conductivity for fast (high C-rate) cycling and minimizing the conducting Carbon additives. Besides that, organic cathode materials should be Lithium-containing in its reduced form, so they can undergo redox reactions directly, similar to current commercial inorganic electrodes. Without prior Li available, it needs Li metal reservoir coming from Li metal anode, which is not feasible due to significant safety concerns related to Li metal dendrite formation, short-circuits, temperature overheating and explosions [46].

Organic positive electrode materials (OPEMs) certainly have garnered significant attention due to the wide range of families and possibilities to explore. These include conducting polymers [39, 47, 48], stable organic radicals such as nitroxides [39, 49, 50], sulphuric compounds [51], conjugated amines [52, 53], conjugated sulfonamides [54], nitro-aromatics [55], oximates [56], disulfonyl methanide [57], and carbonyls [58]. Since most of the reported OPEMs don't contain Li or other alkali metals, it is logical to shift the research focus towards the very few Li-ion containing compounds as listed in fig. 8, which can generate Li reservoir during cycling.

On the other hand, there are currently less reports on organic negative electrode materials (ONEMs), as there is much extensive focus primarily on positive electrode chemistries, which issues and strategies are currently addressed and explored further. Thus, ONEMs have fewer redox families than OPEMs and less specific chemistries, which include (but not exclusively) conjugated dicarboxylates [59], Huckel-stabilized Schiff base [60], Nitrogen-redox azo compounds [61] and the most recently reported N-substituted salts of viologen derivatives [62].

In the Vlad Group, one of the main interests lies on the Li-ion containing cathodes. The current efforts revolve around finding n-type OPEMs that are capable of fulfilling the paramount criteria of a conventional LIB cathodes [63]. A specific class of cathode materials, belonging to the quinone family, is of particular interest due to their high potential, because it has electron withdrawing effect and through-space electronic effect that tunes further the redox voltage beyond normally observed phenomenon, as discussed in the next section [64].

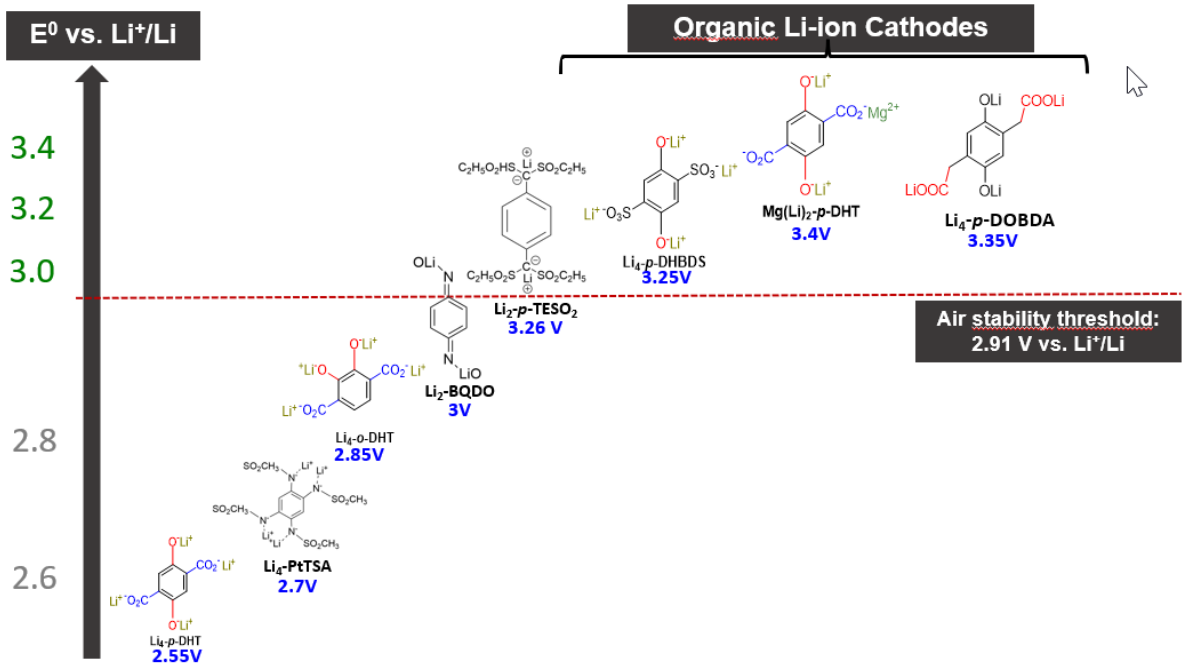

Reversible redox-active moiety	Classification	General redox mechanism	Example of electrode reaction
Conjugated carbonyl	n-type		
Organodisulfide	n-type		
Conjugated azo group	n-type		
Conjugated nitrile	n-type		
Conjugated amine	p-type		
Conjugated etheroxide	p-type		
Conjugated thioether	p-type		
Nitroxide radical	n/p-type (bipolar)		

Fig. 8 Families of organic cathode materials, between 2.55-3.4 V (top) and classification table at the bottom readapted from [35]

II.2.2 N-type Organic Compounds as Cathode Materials

In contrast to p-type compounds, n-type organic materials are compatible with LIB technology, which is why most research investigations are focused on this class of redox molecules [32]. N-type organic materials comprise of these families: quinones, imides, organo-sulphur and oximates [56]. In the

following section, the electrochemical properties and performance of these materials will be described, with a particular emphasis on quinones, due to their promising potential on their energy density value.

II.2.2.1 Quinones

Quinone derivatives are familiar compounds in biological systems, such as plastoquinone and ubiquinone, which play important roles in electron transport processes in vital organs of plants [65]. Prior to the discovery of their solid-phase redox behaviour, quinones in their dissolved liquid phase have shown reversible and rapid two-electron redox reaction kinetics [66]. Similarly, in their solid form, quinones exhibit redox potentials in the range of 2-3 V vs. Li^+/Li. Quinones generally possess high gravimetric, due to their low molecular mass. The combination of high capacity and voltage, contributes to their high gravimetric energy density, leading to increased research interest in this particular class of material [67]. Figure 9 illustrates the formation of semiquinone radical anion intermediate (SQ) during the initial one-electron reduction of p-benzoquinone, which is typically followed by a second electron reduction, resulting in the formation of hydroquinone (HQ) in its deprotonated dianion form (HQ^{2-}). Conversely, the oxidation occurs in reverse, with the negative charges being compensated by two monovalent cations (e.g.: Li^+).

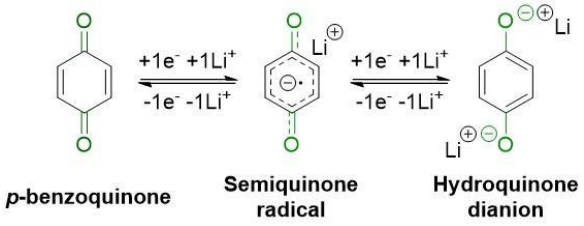

Figure 9: Alleged redox mechanism for quinone derivatives, leveraging on p-benzoquinone example [66].

The investigation of quinones as redox active materials in secondary batteries were originated in 1972, when the electrochemical performance of BQ and its derivatives were intensively studied [67]. BQ/HQ has achieved a very high capacity of 496 mAh g^{-1} compared to other organic redox materials for a two-electron redox couple, with a redox potential of 2.53 V vs. Li^+/Li, as it has low molecular mass of BQ (108 mAh g^{-1}) [34, 67]. However, the superior electrochemical properties cannot be implemented directly in Li-ion cells, as BQ suffers from these 3 main issues: the instability of its radical intermediates, low ionic conductivity and most prominently, high solubility in common battery electrolytes. Ongoing research studies are continuously investigated for this quinone class on addressing these challenges

and optimizing the specific capacity, obtaining high redox potential, while possessing sufficient electrochemical stability over extended cycling periods [68]. These aspects will be expounded in more detail in later chapters, as quinone will be the focus and class of material used for the cathode material.

II.2.3 Tuning the Redox Potential of Quinone Materials

In this section, the focus is on Li-containing compounds (in comparison with some non-Li containing quinones in previous research). The optimization of energy density in electrode materials depend on 2 main parameters: specific capacity and redox potential. By varying the functional/substituted group of quinone derivatives, the chemical nature not only affects their solubility in organic electrolytes, but also their redox potential where reduction and oxidation occurs. The main reason is specifically due to whether it has more of electron-donating or electron-withdrawing functional group, which can decrease and increase the redox potential respectively, as energy level of the highest occupied molecular orbital (HOMO) and lowest unoccupied molecular orbital (LUMO) will be altered [19, 34]. A lower energy level of the LUMO in the oxidized BQ translates into higher electron affinity, which gives higher reduction potential (and vice versa). Similarly, a lower energy level of the HOMO in the reduced HQ corresponds to higher ionization energy and hence, higher oxidation potential. The relation between redox potential and molecular structure of BQ are illustrated below in figure 10:

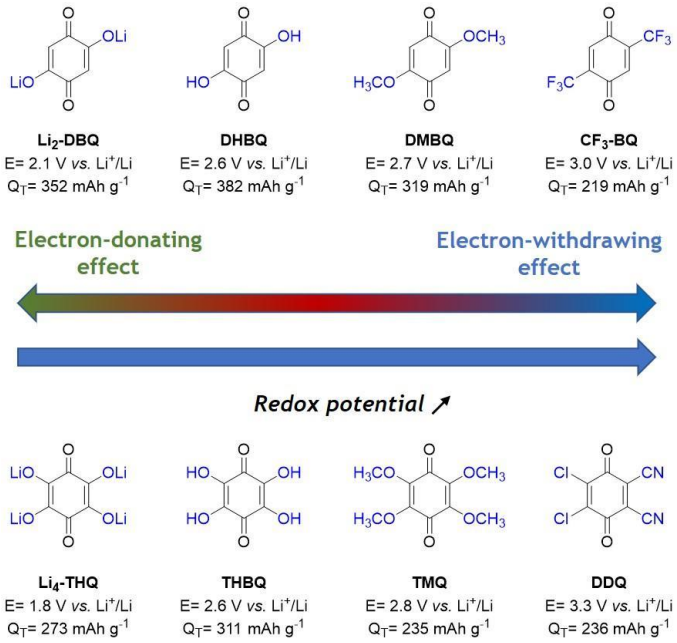

Figure 10: Impact of the electronic effect on the redox potential in BQ derivatives.

Even though negatively charged substitution groups helps to limit the solubility of quinone compounds, but their electron-donating nature simultaneously decreases their working potential, as the redox centre becomes enriched with electron, making it harder to reduce. This is observed in Li_2-DBQ and Li_4-THQ, which have redox potentials of only 2.1 V and 1.8 V vs. Li^+/Li, respectively, as shown in fig. 10. This effect is more pronounced in tetrasubstituted quinone. For instance, replacing the Lithium enolate (-OLi) group by less electron-donating hydroxyl (-OH) groups pushes the working potential higher [69]. The figure conveys the trend of increasing redox potential from left to right, moving from the most electron-donating (EDG) to the most electron-withdrawing functional group (EWG). In EDG, the redox potential increases as the strength of EDG is getting weaker, following this order: -OLi > -OH > $-OCH_3$. EWG is presented by highly electronegative elements such as halogens (Cl, F) due to negative inductive effect and by the nitrile (-CN) group that has negative mesomeric effect. These electron withdrawing effects further decrease the energy level of the HOMO, which increases the redox potential, as evidenced by the higher potential of CF_3-BQ and DDQ in the right side.

II.2.4 Novel High Energy Density Quinone Material with Li Reservoir to Boost Electrochemical Performance

With all the progress accumulated, organic battery materials should fulfil these paramount criteria: a Li-ion cathode chemistry which is stable in its reduced phase, Li-containing and stable in ambient air, which allows easy and cost-effective processing industrially similar to its inorganic counterparts, as it can be scaled up more efficiently. Unlike the anode, which has lower redox potential and, in its Li-free oxidized form, the cathode requires to be Li-containing to avoid depleting Li^+ ions from the carrier salt in the electrolyte. Not only that, Li metal anode is unsafe as it tends to form dendrite that pierce separator and causing short-circuits upon repeated cycling.

Most organic compounds are also extremely reactive towards oxygen and moisture, which is impractical in their handling. Achieving air stability is only possible when it passes the threshold value of 2.91 V vs. Li^+/Li as its end-of-discharge potential (or preferably above 3 V) [83]. Even though there are organic battery chemistry above this voltage, the redox mechanism is based on cationic species upon oxidation, and need to be compensated by anions, which deviates from the conventional Li-ion design [84]. Hence, more research needs to be done to achieve this high redox potential compound, with poor solubility in organic solvent (to minimize capacity fading), and demonstrate good cycling stability. In the next section, the compound Li_4-*p*-DOBDA will be discussed as a potential choice for the cathode material.

Redox potentials can be influenced by inductive or mesomeric effects. Quinones with electron-deficient properties, as shown in fig. 11, have proven to boost the redox potentials higher. The first compound that has been reported by Lakraychi *et al*. is on 2,5-dihydroxy-1,4-benzenedisulfonic acid (Li_4-*p*-DHBDS) with a redox potential of approximately 3.25 V vs. Li^+/Li, making it stable under dry air, but not resistant to moisture [70]. However, irreversible insertion and extraction processes lead to capacity fading as the compound cannot provide full capacity after the first cycle, which is inherent stability issue. In a similar timeframe, Jouhara *et al*. improved the redox potential of p-DHT_4^- by substituting Lithium with other spectator cations, modifying electronegativity, that leads to a higher voltage gain reaching 3.4 V vs. Li^+/Li [71]. However, this compound allows only single-electron insertion and extraction, limiting its capacity. The redox potential increase of these compounds can be explained by through-bond electronic effect, which is correlated to increase or decrease in their charge density, following by decrease of increase in their redox potential [64]. Nevertheless, the redox potential increase can be compromised by reduction in capacity, as different substituents have different molecular weight, especially when higher molecular weight, leads to inferior specific capacity.

Li_4-*p*-DOBDA, with a similar structure to Li_4-p-DHT exhibits higher potential difference. The effect responsible for this increase is not solely through-bond electronic effect, since according to this effect, the potential should rest between 2.55 – 2.8 V vs. Li^+/Li. This investigation was conducted similarly by adjusting the functional group from the para to the ortho position of Li_4-p-DHT to Li_4-o-DHT, resulting in a gain of 0.3 V in the latter compound, despite having identical chemical structure and negative dipoles, differing only in the position of carboxylate group [72]. Similarly, Li_4-*p*-DOBDA exhibits a higher redox potential (of 3.35 V vs. Li^+/Li) due to through-space intramolecular electronic charge modulation. The observed 650 mV increase is attributed to electrostatic interaction not from two enolates group, but of neighbouring enolate (-CO^-Li^+) and carboxylate (-$CH_2COO^-Li^+$) groups [64]. This redox potential boost is achieved through the donor inductive effects (+I) from the acetate groups, which influence the electronic density of the aromatic cycle. In addition, acetate groups in $DOBDA^{4-}$ enable structural flexibility, which displays stereoelectronic chameleonic behaviour which depends on its counter-cation [64]. In addition, this effect can also be extended to post-Li ion batteries with other Alkalis such as Na, K, Ca and Mg.

II.2.4.1 Li_4-*p*-DOBDA

The scarcity of Li-ion organic cathode materials with comparable electrochemical performance to their inorganic counterparts, while remaining stable in ambient air in a reduced lithiated state, highlights

the need for rigorous research direction in this field. Addressing this gap would enable OBs to be processed similarly to conventional LIB positive electrodes. A recent discovery by Louis Sieuw *et al.* from Vlad Group introduces a promising material known as tetralithium salt of 2,5-dihydroxy-1.4-benezediacetic acid (Li_4-*p*-DOBDA). Its chemical structure, depicted in fig. 11, bears resemblance to tetralithium 2,5-dihydroxyterephthalate salt or known as Li_4-p-DHT [64]. Both compounds possess permanent negative charges dipoles coming from hydroxyl and carboxylate groups that augments its polarity [73-75]. Li_4-*p*-DOBDA manifests these attractive properties worth exploring further: it undergoes a reversible two-electron electrochemical reaction with a 0.8 V redox potential higher than Li_4-p-DHT (3.35 V vs. Li^+/Li), possesses high energy with a theoretical capacity approaching 215 mAh/g and shows no signs of degradation by oxidation or hydrolysis even after prolonged exposure, rendering it air-stable. This phenomenon is further supported by electrochemical testing, crystallography analysis, comparative infrared spectroscopy (IR) and DFT calculations [64]. Although optimizations are necessary ranging from its electrode formulation, cell design, cycling stability, as well as mitigating solubility and polarization issues (which focus will be explored further), this organic battery chemistry reveal a lucrative potential to challenge the conventional inorganic LIB chemistries, with gravimetric energy density is in similar range to $LiFePO_4$ (LFP) and $LiCoO_2$ (LCO).

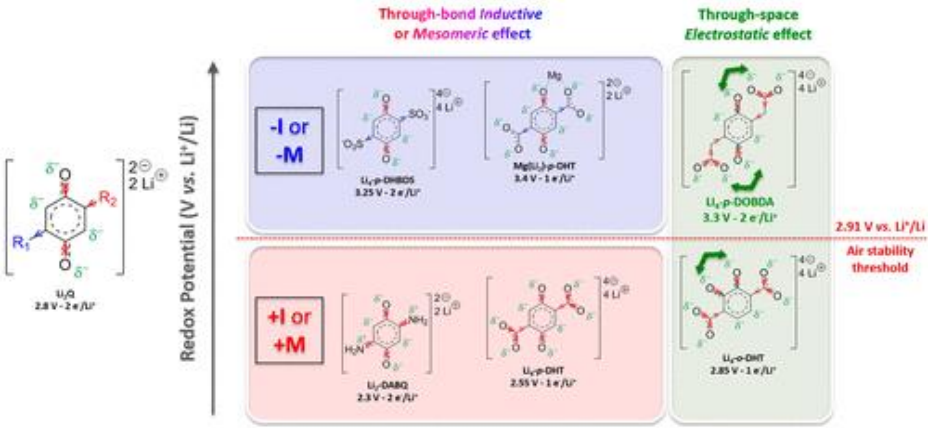

Fig. 11 Conventional through-bond electronic effect is observed in both electron-deficient quinones with increased redox potential, or electron-rich systems with lower redox potential [85]. However, through-space electrostatic charge and redox potential modulation possibly overrides the through-bond effects which electrode emerges with higher redox potential than expected.

Li_4-*p*-DOBDA, as n-type organic cathode that belongs to quinones, has similar characteristics with the conjugated sulfonamide (CSA) class due to its intrinsically high potential. CSA chemistries have

exhibited varying potential between 2.85-3/45 V vs. Li^+/Li with flexibility to tune its electrochemical performance [54]. Li_4-DOBDA can reversibly accept and gives 2 electrons upon reduction and oxidation ($Q^0 \leftrightarrow Q^{2-}$), as shown in fig 11 above. However, direct use of BQ is not feasible, despite its high theoretical energy density of 440 mAh/g at redox potential of 2.7 V vs. Li^+/Li, as reduced Q^{2-} is sensitive to oxidation in air, while oxidized state of Q^0 is highly soluble in common electrolytes [90]. Incorporating amines into the substituted functional groups of quinones, as it has low molecular weight, can reduce the solubility issues, but typically results in lower redox potentials which comes as inevitable compromise due to its more electron-donating nature and overall chemical structure as the carboxylate groups are substituted [91]. In addition, Li_4-*p*-DOBDA benefits from n-type material redox process, unlike other organic battery chemistries above 3 V vs. Li^+/Li that depend on the removal of anions or p-type redox, which is not suitable for conventional LIB chemistry.

Electrochemical performance of Li_4-*p*-DOBDA can be improved with particle size reduction as there is more surface area contacts between each particle and larger percolation network for ionic and electronic conduction. It has been demonstrated that by making nanostructures, capacity can be improved, while simultaneously reducing polarization [76]. Hence, the focus in the next section would be on implementing particle size reduction techniques for Li_4-*p*-DOBDA.

II.3 Downsizing Particles Strategies

Organic molecules of BQ families have shown to have high potential, but in expense of its specific capacity and cycling stability, namely its solubility and polarization issue [77]. Recent research has demonstrated that nanostructures and nanocomposites of organic conducting polymers offer numerous active sites with better kinetics, due to its facile electronic/ionic transfer and diffusion [78]. Transitioning from bulk to nanostructured electrode materials is the key to create green and sustainable battery that offers large capacity, high energy and power density, high efficiency and long cycle life [79].

There are several strategies to reduce the polarization and solubility issue by reducing particle size, which also improves kinetics. Using the example of 2,5-dihydroxyterephthalic acid, $Li_4C_8H_2O_6$ (DHTPA), it was found the capabilities of electrochemical performance in the following order: nanosheets > nanoparticles > bulk [76]. There are 2 strategies to obtain this nanostructured, by using sonication to create nanosheets structure and ball-milling to create nanoparticles as their microstructure was shown by SEM images in figure 12 below.

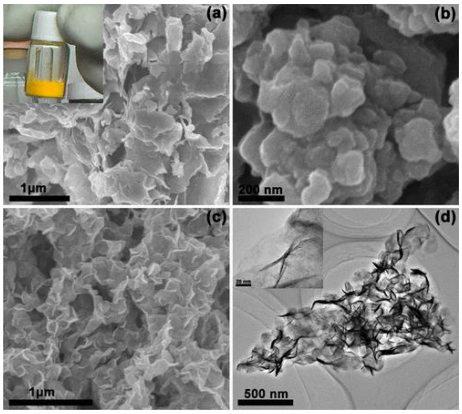

Fig. 12 SEM images of $Li_4C_8H_2O_6$ in (1.) bulk, inset shows the powder in glass vial, (b.) nanoparticles, (c.) nanosheets. (d.) TEM image of $Li_4C_8H_2O_6$ nanosheets with inset of single nanosheet layer [76].

Organic nanoparticles were obtained by mixing the organic active material electrode, conductive carbon and binder in specific ratio, inside a stainless-steel container for ball-milling, along with several stainless-steel balls of specific diameters. The composite particles were then uniformly mixed during the process, resulting in reduced particle size. A set of frequency and time setup were applied to crush and reduce the particle size of the composite, with uniform particle size preferred to allow homogeneous properties across throughout the sample.

Organic nanosheets were obtained through the ultrasonication of the molecule by exfoliating a single layer (like graphene) in a protic solvent, such as methanol. The interaction with protic solvent, through dispersion effect and solvent molecule coordination to the Li-ion of tetralithium salt facilitated the formation of nanosheets [76].

Within 1.8-3.2 V potential range, DHTPA exhibited high first charge and discharge capacities of 226 and 223 mAh g^{-1}, with Coulombic efficiency sufficiently close to 99.9% [76]. On the other hand, the bulk material only showed 148 and 145 mAh g^{-1} for its first charge and discharge capacity, respectively, with 94% capacity retention after 50 cycles [76]. The nanoparticles performed better compared to the bulk, but its reversible capacity is slightly inferior to nanosheets' measurement [76]. Overall, the organic nanosheets has shown the best electrochemical performance among the 3 profiles with an initial discharge capacity of 223 mAh g^{-1} and capacity retention above 95% after 50 cycles at a 0.1 C rate [76]. This can be attributed to the 2D nanosheets providing shorter Li^+ diffusion pathway and a larger contact area for both conducting agent and electrolyte, increasing its ionic conduction. However, beyond 50 cycles there was a more rapid capacity fading due to structural or morphological material changes during cycling or material solubility issue that needs to be further addressed when working with Li_4-*p*-DOBDA in this project.

III. Objectives and Scope

Li_4-*p*-DOBDA is chosen as organic cathode for LIB due to its high redox potential and high specific theoretical capacity as a member of quinone family. It can accept and release 2 e^- and 2 Li^+ upon discharging (reduction) and charging (oxidation), respectively with average redox potential of 3.35 V (as it occurs on 2 different redox potential level of 3.25 V and 3.45 V) as shown in fig. 13. Further oxidation to tetralithium salt leads to irreversible structural/phase transition. Nevertheless, Li_4-*p*-DOBDA full capabilities as OPEMs are still overshadowed by its polarization (the potential difference where charge and discharge happen) and solubility issues. Besides that, considering the decreasing Li supply and exponentially increasing Li demand, it is important to explore the chemistries, electrochemical performance and possible alternative solution in post Li batteries (Na, K, and can be extended to Ca and Mg) using Li_4-*p*-DOBDA, which are not explored thoroughly yet. This thesis aims on investigating these issues to optimize the material by reducing polarization and solubility, that can be characterized by the potential difference where charge and discharge occur and the rate at which capacity fades over subsequent cycles.

My objectives are defined as follows:

1. Optimization of material properties and electrochemical performance of downsized Li_4-*p*-DOBDA.
2. Preliminary investigation on the chemistry and exotic redox phenomena of Li_4-*p*-DOBDA which system is transferrable to post-LIB (Na, K, Mg, Ca, etc)

Several optimization protocols for downsizing the molecule to nanostructure will be discussed, before verdict on the best techniques for this particular case is taken. The physicochemical material properties can be defined from its morphology, particle size, crystal structure, uniformity and purity of the formed molecule, will be characterized. Electrochemical characterization can be measured by its specific capacity (especially during cycling), cycling stability, Coulombic efficiency and polarization. When the system has been optimized in LIB, Li_4-*p*-DOBDA can be transferred as organic cathode for post-LIB system, such as in Na and K batteries, which will be discussed later in the next section.

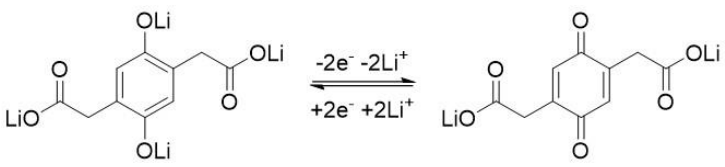

Fig. 13 Charge and discharge reversibility upon redox process of Li_4-*p*-DOBDA

IV. Materials and Methodology

Experimental Protocols

IV.1 Synthesis of the tetralithium salt of 2,5-dioxy-1,4-benzenediacetic acid (Li_4-*p*-DOBDA)

IV.1.1 Inert atmosphere (inside glovebox)

In an Argon (Ar)-filled glovebox, to a solution of 565.45 mg (2.5 mmol, 1 eq) of 2,5-dihydroxy-1,4-benzenediacetic acid (H_4-p-DOBDA, 97% Sigma Aldrich) in 20 mL of anhydrous methanol (CH_3OH, >99.9% Sigma Aldrich) was prepared. To this solution, 379.7 mg (10 mmol, 4 eq) of Lithium Methoxide ($LiOCH_3$, 98% Sigma Aldrich) was added. The resulting mixture was stirred for at least 24 hours at room temperature and led to the precipitation of a beige powder. The solid then was retrieved in the glovebox by centrifugation for at least 3 rounds of 3 minutes at 6000 rotations per minute (rpm) and washed with anhydrous methanol (Sigma Aldrich) prior to centrifugation. The powder was subsequently dried under reduced pressure at 120^o C for 3 hours, resulting in the collection of 549.8 mg (2.5 mmol, 1 eq) of pure Li_4-*p*-DOBDA (yield = 88%).

IV.1.2 Ambient Atmosphere, Ar-purged (inert, Schlenk tube method)

To a solution of 565.45 mg (2.5 mmol, 1 eq) of H_4-*p*-DOBDA (97% Sigma Aldrich) in 20 ml of methanol (Sigma Aldrich), 559.85 mg (10 mmol, 4 eq) of Lithium Hydroxide monohydrate ($LiOH.H_2O$, >98% Sigma Aldrich) were added. The mixture was stirred at room temperature for 24 hours and led to the precipitation of a beige powder. With the aid of Schlenk tube and both Ar and vacuum purging, the solid was retrieved by filtration using a Millipore PVDF 0.45 µm hydrophilic filter, and then washed with at least 60 mL methanol (Sigma Aldrich), followed by a final wash with diethyl ether to remove any excess methanol. The obtained powder was dried overnight under reduced pressure at 70^o C. As a result, 448.6 mg (2.5 mmol, 1 eq) of pure Li_4-*p*-DOBDA was collected (yield = 71.8%) [64].

IV.1.3 Ambient Atmosphere (without Ar purging)

Li_4-*p*-DOBDA was also synthesized under ambient atmospheric condition. The pristine Li_4-*p*-DOBDA was obtained through reaction of 565.45 mg (2.5 mmol, 1 eq) of H_4-*p*-DOBDA (97% Sigma Aldrich) in 20 ml of methanol (Sigma Aldrich) with 559.85 mg (10 mmol, 4 eq) of Lithium Hydroxide monohydrate

($LiOH.H_2O$, >98% Sigma Aldrich). The mixture was stirred for 24 hours at room temperature to yield the beige tetra-lithium salt. The solid was recovered by filtration using a Millipore PVDF 0.45 µm hydrophilic filter, and washed with at least 60 mL methanol (Sigma Aldrich), followed by a final wash with diethyl ether to remove any excess methanol. The powder was then dried overnight under vacuum at 70° C, and subsequently 269.9 mg (2.5 mmol, 1 eq) of pure Li_4-*p*-DOBDA were collected (yield = 43.2%). The low yield was caused by presence of dissolved oxygen and the unstable oxidized dissolved phase, as indicated by the rapid colour changes to dark yellow/brown in this method.

IV.2 Preparation of Na_4-*p*-DOBDA and K_4-*p*-DOBDA (Inert Atmosphere inside Glovebox)

In an Ar-filled glovebox, to a solution of 90.47 mg (1 mmol, 1 eq) of 2,5-dihydroxy-1,4-benzenediacetic acid (H_4-*p*-DOBDA, 97% Sigma Aldrich) in 20 mL of anhydrous CH_3OH (>99.9% Sigma Aldrich) was prepared. To this solution, 216.12 mg (4 mmol, 4 eq) of Sodium Methoxide or 408.68 mg (4 mmol, 4 eq) Potassium Methoxide ($NaOCH_3$ or $KOCH_3$, 98% Sigma Aldrich) were added. The mixture was stirred for at least 24 hours at room temperature, which led to the precipitation of a beige powder. The solid then was retrieved in the glovebox by centrifugation for at least 3 rounds of 3 minutes at 6000 rotations per minute (rpm), followed by washing with anhydrous methanol (Sigma Aldrich) before being centrifuged again. Subsequently, the powder was dried under reduced pressure at 120° C (for Na_4-*p*-DOBDA) or 200° C (for K_4-*p*-DOBDA) for 3 hours, and 251.3 mg (1 mmol, 1 eq) of pure Na_4-*p*-DOBDA or 302.8 mg (1 mmol, 1 eq) K_4-*p*-DOBDA were collected (yield = 80%).

IV.2 Downsizing Electrode Particle Size with Ball-Milling and Composite Electrodes Preparation

IV.2.1 Li_4-*p*-DOBDA Composite Using Ball-Milling

Sixty mg of Pristine Li_4-*p*-DOBDA powder was premixed with 30 mg SP Carbon Black (TIMCAL) in 2:1 mass ratio ($m_{tot.}$ = 90 mg) using a high energy Anton Paar Ball-mill. The ball milling process was conducted three times for 15 minutes each, with 20 minutes rest in between. The ball mill operated at 25 Hz, and fifteen 3 mm (diameter) stainless steel balls were used along with stainless steel containers. PTFE binder (10 mg) was added to the final mixture ($m_{tot.}$ = 100 mg), and the ball milling process was repeated to give the final formulation with the following mass ratio: Li_4-*p*-DOBDA: SP: PTFE = 6:3:1. The mixture was then pressed on a stainless-steel grid (AISI 316L) with 10T pressure to

form the working electrode inside a glovebox. A typical cathode was composed of 1.5-2 mg of composite.

In the case of sample with 10%Graphene, 60 mg of active material was premixed with 10 mg graphene (Global Graphene Group) with 6:1 mass ratio ($m_{tot.}$ = 70 mg) with similar settings above, and then 20 mg of SP and 10 mg of PTFE were added before repeating the ball milling process. The final formulation resulted in the following ratio: Li_4-*p*-DOBDA: Graphene: SP: PTFE = 6:2:1:1, ensuring that the total carbon material remained at 30% of the composite mixture. When 5 Hz Ball mill setting was selected, the process remained identical, with the exception of choosing 5 Hz during the ball milling process. This yields 4 different profiles to analyse further: SP 5 Hz, SP 25 Hz, G-SP 5 Hz and G-SP 25 Hz.

IV.2.2 post-Li DOBDA, hand-grounded composite formation

For pristine Na_4-*p*-DOBDA or K_4-*p*-DOBDA, the active material was ground and premixed with SP Carbon Black (TIMCAL) and PTFE binder in 6:3:1 mass ratio ($m_{tot.}$ = 100 mg) using mortar and pestle for at least 15 minutes. The mixture was then pressed onto a stainless-steel grid (AISI 316L) with 10T pressure to form the working electrode inside a glovebox. A typical cathode was composed of 1.5-2 mg of active material.

IV.3 Material Characterization Techniques

IV.3.1 Fourier-Transform Infrared (FTIR) Spectroscopy

FTIR spectra were produced for the pristine powders (Li, Na and K compounds) and their respective composites, by using Agilent Technologies Cary 630 spectrometer with a single reflection ATR module, conducted inside a glovebox.

IV.3.2 Powder X-ray diffraction (PXRD)

PXRD data were acquired on STOE Stadi P diffractometer in Debye-Scherrer equipped with a Mo anticathode (Kα radiation), that operates at 50 kV and 40 mA.

IV.3.3 Scanning Electron Microscopy (SEM)

SEM images were captured on using a JEOL JSM-7600F Microscope with varying resolution and magnification size.

IV.4 Electrochemical Characterization Methods in Two-Electrode Coin Cell Configuration

IV.4.1 Galvanostatic charge discharge (GCD)

The solid phase electrochemical performances of Li_4-*p*-DOBDA and Na_4-*p*-DOBDA were evaluated in a half-cell configuration using a two-electrode coin cell, assembled as shown in figure 14, in an inert, Ar-filled glovebox. The coin cell was assembled bottom up, starting from the cathode case, then proceeded upwards to the composite Li_4-*p*-DOBDA with distinct profiles, separator, followed by stainless-steel current collector, spacer and anode case. The resulting composite electrode from the previous section was used as working electrode. A Li metal foil disk (Alfa Aesar) was used as reference and counter electrode. Furthermore, a single sheet of Whatman grade GF/D glass microfiber filter was used as separator between the working electrode and Li disk. Fifty µL of battery grade 1M $LiPF_6$ in EC: DEC (1:1) electrolyte for Li cell, or 1M $NaPF_6$ in EC: DEC (1:1) for Na cell was employed to soak and wet in the separator. The cells were assembled further according to the configuration shown in figure 14 below, and cycled at a rate of 2 Li^+ (or 2 e^-- exchange per 10 hours (or equivalent to 0.1 C rate, wherein 1C corresponds to 214.51 mAh/g). For Na cells, Li chip is substituted with a thin Na metal sheet for the anode instead. The galvanostatic measurements were recorded using a Biologic VMP potentiostat and Neware battery cycler (shown in the appendix).

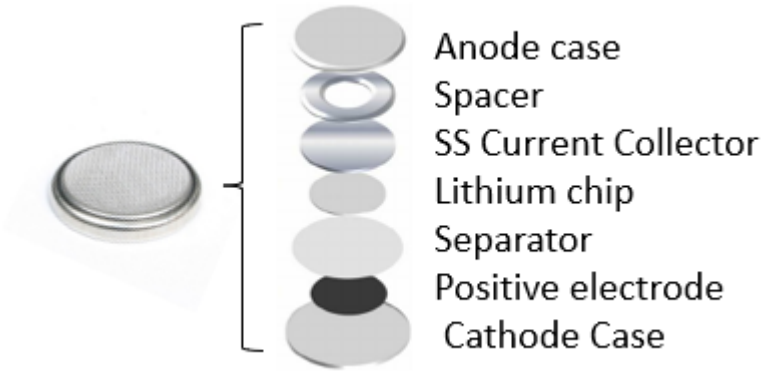

Figure 14. Assembly of Half-cell of coin cell with Li anode

IV.4.2 Potential and Capacity Limitation Setup in GCD for Li-reservoir Formation

The capacity and potential are limited to prevent solubility at higher voltages beyond 3.9 V, characterized by extra humps and over-capacity beyond its theoretical capacity in Voltage-Capacity curve. This setup, as shown in table 1 aimed to reduce solubility issues, as evidenced by capacity fading and minimize polarization, not only during the first cycle but also throughout the cycling process. For an example of calculation, Li_4-*p*-DOBDA electrode with mass of 2 mg is used, so active mass with 60% of total mass will give 1.2 mg. After multiplying this active mass with its theoretical capacity, this brings its max capacity limited at 257.41 mAh. The calculated current for 0.1 C rate is obtained by dividing 10 hours of the previous value, which is 25.74 mAh for both charge and discharge.

Table 1 GCD Setup for Cell Electrochemical Performance Optimization, Limited Cycling at C/10 Rate

ID	Step name	Step time (hours)	Voltage (V)	Current (mA)	Capacity (mAh)
1	Rest	3			
2	Charge		3.9	Capacity/10	TC * active_mass
3	Discharge		2.7	Capacity/10	
4	Cycle	Begin ID: 2		Times: 99	

Active mass = electrode mass * 60%

Theoretical capacity:

Li_4-*p*-DOBDA = 214.51 mAh/g, Na_4-*p*-DOBDA = 85.33 mAh/g

V. Results and Discussion

V.1 Li_4-*p*-DOBDA

Based on the findings presented in the previous chapter, Li_4-*p*-DOBDA is chosen as the focus of this study because of its favourable characteristics such as high specific capacity and high voltage above air stability threshold, similar to LFP [64]. Furthermore, it also demonstrates higher redox potential through-space charge modulation as its 3D arrangement in space changes. The redox potential is curiously higher in the solid state (where the functional group of enolate and acetate are closer, giving more electrostatic repulsion) compared to the solution phase, when the neighbouring functional group is more far apart and has weaker repulsion.

Inspired by the previous work written in Louis Sieuw's thesis, it was observed that despite its high first cycle discharge capacity of 147.2 mAh/g and redox potential achieved for Li_4-*p*-DOBDA cell, it has issues with high polarization, as well as rapid capacity fading due to solubility issue. Previous GCD test was done when this compound was made into composite with KB carbon as depicted below in figure 15. However, polarization of 0.471 V during the first cycle and rapidly declining capacity to just 36.7 mAh/g at 10^{th} cycle clearly proves the solubility issue that makes it unsuitable for long-term cycling.

Also, it is worth noting that carboxylates have a recommended upper potential cut-off is less than or equal to 4 V to avoid decarboxylation, which leads to the capacity fading, irreversible redox reactions and possibly forming other undesirable soluble side-reaction products. In the previous study by Louis *et al*., KetjenBlack (KB), was the conductive carbon utilized [64]. KB is a graphitic carbon which has capacity contribution between 2.7-3.9 V vs. Li^+/Li, so it will become challenging to accurately and precisely determine the fraction of capacity solely attributed to Li_4-*p*-DOBDA alone. Hence, other carbon material will be considered. In subsequent electrochemical study, GCD testing will be performed using SP carbon (which has negligible to no capacity contribution above 1.5 V vs, Li^+/Li), as well as the setup of limiting capacity at its theoretical capacity and limited potential at 3.9 V to avoid it being cycled at this region. SP carbon also has smaller particle size which potentially lowers the polarization issue further in contrast to the graphitic KB structure. Its cycling stability curves for hand-grounded cell using SP and KB carbon are given in the appendix at fig. A6 as reference.

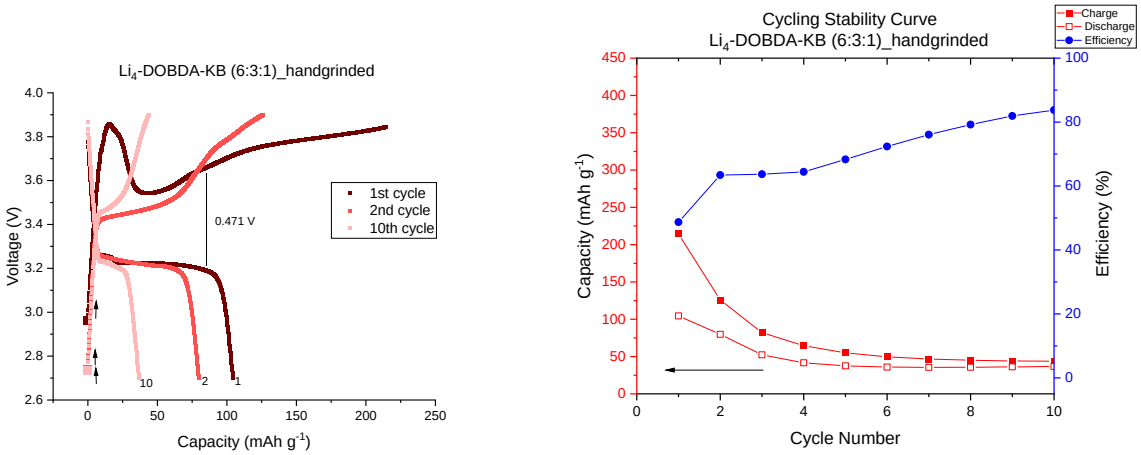

Fig. 15 GCD Profile of Li_4-*p*-DOBDA KB (6:3:1) for the first 10 cycles, Voltage-Capacity curve (left) and Cycling Stability over 10 cycles (Right)

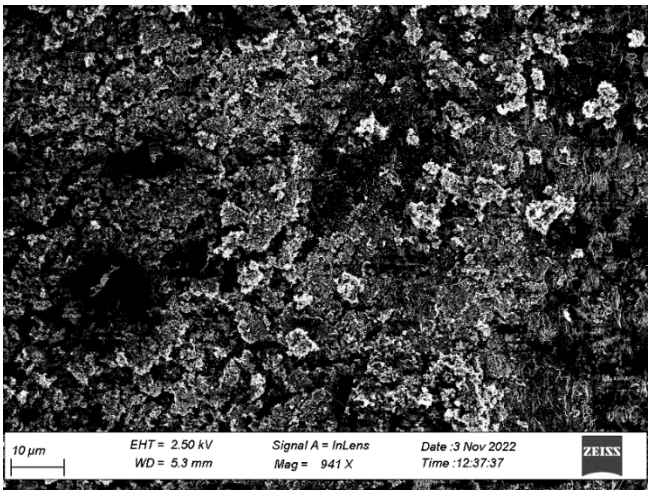

Fig. 16 Morphology and topography of Li_4-*p*-DOBDA with KB (6:3:1) under SEM

Furthermore, SEM result reveals that the Li_4-*p*-DOBDA composite with KB exhibits irregular non-uniform particle with an average size of 5 µm (4-6 µm), in which it does not solve the polarization and solubility issues, as well as the material can behave irregularly depending on which portion of the composite powder was analysed. Therefore, downsizing the particle size can be beneficial as it will increase surface area of the contacts between particles and improves uniformity, which will be discussed in the next section. The next composites that will be discussed will contain SP for the aforementioned reasons.

V.1.1 Synthesis and characterization of Li_4-*p*-DOBDA

The synthesis of Li_4-p-DODBA involves acid-base reaction, where the ligand H_4-*p*-DOBDA that acts as acid, and $LiOCH_3$ that acts as base, as there is deprotonation by $LiOCH_3$ base exchange of cation (in this case, Li^+ ion) to form the final compound. This reaction is commonly known as a neutralization reaction, resulting in the formation of the salt Li_4-*p*-DOBDA and methanol. This method will be similar for whichever alkali or alkali earth ions used to form the final alkali compounds. Typically, redox active organic molecules are synthesized inside inert Argon atmosphere within a glovebox. However, due to the air stability of Li_4-*p*-DOBDA, it also can be synthesized under ambient air, or outside the glovebox but purged with Ar to protect it from oxidation or moisture interference, before the ligand H_4-*p*-DOBDA fully reacted with the sample. When synthesized under ambient air, the compound will turn into a darker brown colour due to reaction with O_2 and H_2O as shown in Fig. A9, compared to beige colour that is retained longer for other methods. The exact steps can be referred in the experimental methods section.

Initially, the synthesis was done under ambient air conditions to investigate the air stability of the compound, in comparison with Schlenk tube method as shown in the fig. 17 below. In Schlenk tube method, the compound was synthesized entirely under an Ar atmosphere condition since both precursors were mixed to avoid even a slight oxidation that can create instability of the partially oxidized H_4-*p*-DOBDA that affects the final yield and purity of the sample, such in the case of ambient air synthesis condition.

Fig. 17 Li_4-*p*-DOBDA synthesis utilizing Schlenk tube method

Air processability is an important parameter for battery manufacturing, especially for Li cathode materials. Since Li_4-*p*-DOBDA has redox potential above 3V vs. Li^+/Li, similar to LFP, the compound will be resistant to oxidation in the air, but not necessarily to moisture. The air stability is investigated between the ambient-air synthesized (after at least a week) vs. Schlenk tube method to investigate if there is any difference of the resulting compound, using both XRD and FTIR techniques.

However, based on the XRD data (for ambient air synthesis, at least exposed in ambient air for a week) in the fig. A2 in the appendix between both methods, it is revealed that resulting product from both methods are shown an identical pattern, proving its air stability of Li_4-*p*-DOBDA as its average redox potential of 3.35 V is higher than oxygen reduction potential of 2.91 V vs. Li^+/Li. However, the yield for ambient air synthesis method is less than half (43.2%) compared to Schlenk tube (71.8%) and glove box synthesis (88%) method. Even Louis *et al*. reported far lower yield of 15% using ambient air synthesis method. The low yield is caused by presence of dissolved oxygen and presence of trace water in solvents that oxidized the dissolved phase, which is instable and highly reactive (in its ligand form). Therefore, the synthesized Li_4-*p*-DOBDA discussed in the following section will be based on the Schlenk tube or glovebox synthesis method.

Based on the obtained XRD pattern and FTIR spectra of Li_4-*p*-DOBDA synthesis done under ambient air and using Schlenk-tube method, there is no noticeable difference due to identical shape and pattern obtained, indicating that Li_4-*p*-DOBDA remains stable even after prolonged exposure to ambient air. The crystal structure and its chemical composition are maintained despite exposure to air. However, since the yield of Ar-purged Schlenk tube and glovebox synthesis method are higher, with 71.8% and 88% respectively, compared to air synthesis with only 41%, hence for efficiency the material and cell characterization will be based on the inert atmosphere using Schlenk-tube method (and for practical reasons, it had been done earlier and show negligible difference besides slightly lower yield to the glovebox synthesis).

Finally, the last synthesis method was done inside glovebox, which instead of filtering, the sample was centrifuged to make concentrated wet powder separated from the solvent (Methanol) before being dried. Due to low oxygen and water content in glovebox (<0.1 ppm), the compound was guaranteed to be pure and grants higher yield than the other 2 methods previously mentioned.

V.1.2 Li_4-*p*-DOBDA Bulk and its Electrochemical Performance

After the synthesis was done, the physicochemical and electrochemical properties need to be evaluated further. SEM analysis of the bulk Li_4-*p*-DOBDA reveal a plate-sheet like morphology of

particle size between 1-2.5 μm with a mean size 2 μm, which is non-uniformly dispersed throughout the sample below in figure 18. This doesn't guarantee similar electrochemical properties, as the size difference affects the capacity, polarization and cycling stability. The case is even more pronounced for hand-grinding with SP, where larger agglomeration and even wider variable particle sizes distribution ranging from 1.8 – 21 μm with mean size of 7.6 μm are observed.

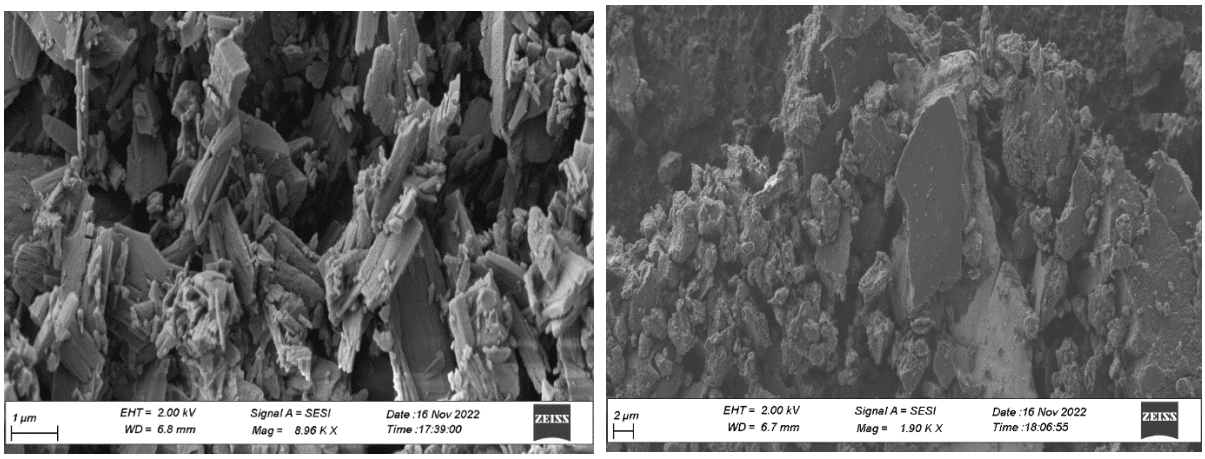

Fig. 18 SEM micrographs of Li_4-*p*-DOBDA for a.) bulk (left) and b.) SP composite (right)

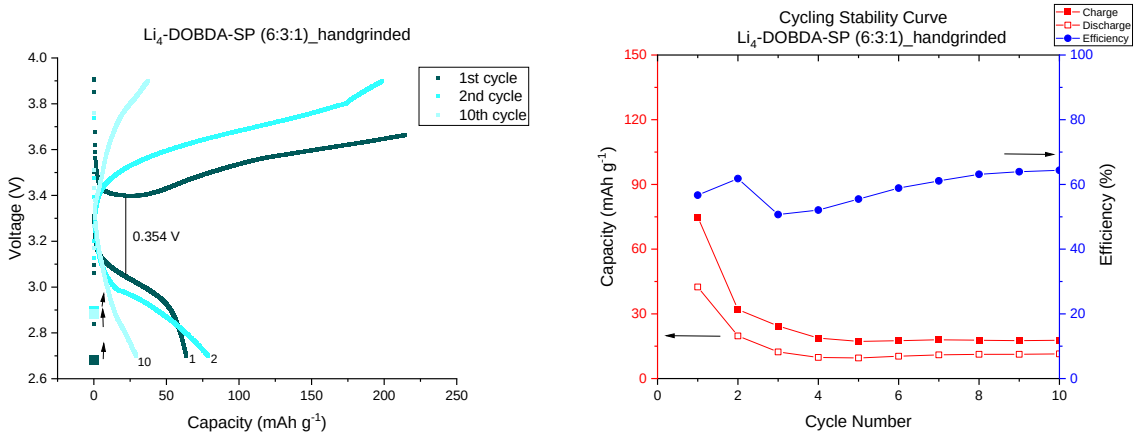

Fig. 19 GCD of hand-grounded Li_4-*p*-DOBDA SP composite

When the hand-ground SP composite sample was made into a cell, the capacity and its cycling stability are unsatisfactory. Its first cycle discharge capacity only reaches 63 mAh/g, while it fades to 29 mAh/g at 10th cycle, which indicates around 63% capacity reduction in just a short period of cycling between 2.7 – 3.9 V vs. Li^+/Li, which can be attributed to its solubility issue. Although it has better polarization by cutting roughly a quarter of the polarization from 0.471 V using KB composite to 0.354 V in SP

composite, however this is far from optimal as good cell should has minimal polarization. The solubility issue that causes polarization and capacity fading are revealed through the photos of cycled Li_4-*p*-DOBDA on both sides as shown in fig. 20 below. Furthermore, its first cycle discharge capacity is far from reaching its first cycle charge capacity that hits its theoretical capacity (after being limited in both capacity and potential, refer to experimental method section). Thus, there are still significant rooms for improvement to achieve the objectives of this project. This is where downsizing the particles into a nanostructure becomes crucial in order to achieve the goals mentioned previously in the objectives.

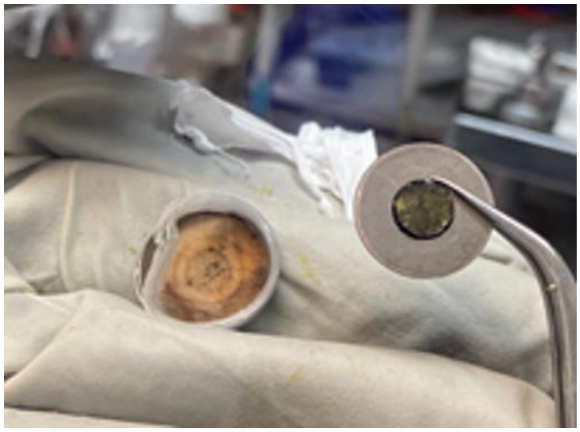

Fig. 20 Solubility issue in cycled Li_4-p-DOBDA at separator (electrode side, left) and the active cathode material at cathode case side (right)

V.1.3 Downsizing Li_4-*p*-DOBDA Strategies to Improve Electrochemical Performance

V.1.3.1 Ultrasonication

Organic nanosheets were proven by Jun Chen *et al.* to have the best capacity and cycling stability, as discussed previously [77]. However, it remains unclear whether nanosheets or nanoparticles will be more effective nanostructure in the chosen Li_4-*p*-DOBDA, as well as yielding better properties and performance. Both techniques aim to reduce the particle size, but through different pathways. Ultrasonication reduces size by exfoliation of the particles into single-sheet particle similar to graphene, while Ball-milling applies high-energy vibrations at selected frequency to impact and give attrition, resulting in nanoparticles formation.

Firstly, ultrasonication will be discussed to create nanosheets. There are 2 ways to sonicate, either using normal sonication (NS) or probe sonication (PS) which reference photos are shown below in fig. 21. In normal sonication, only the top layer samples were taken for SEM analysis, once the larger

particles settled down. Similarly, in probe sonication, the samples were centrifuged after approximately 16- 20 minutes sonication, to allow the particles to settle. Then, the samples were dried at 70^{o} C overnight to remove excess methanol. Both XRD and FTIR analysis do not show any significant difference with the pristine sample, which established their mechanochemical stability. However, SEM analysis reveals agglomeration of large particle sizes and non-uniformity throughout the sample. The NS sample exhibit particle size of approximately 3.7 μm, while PS sample display particle size ranges from 1.67 to 3.65 μm, which are still relatively large enough and prone to possible agglomeration.

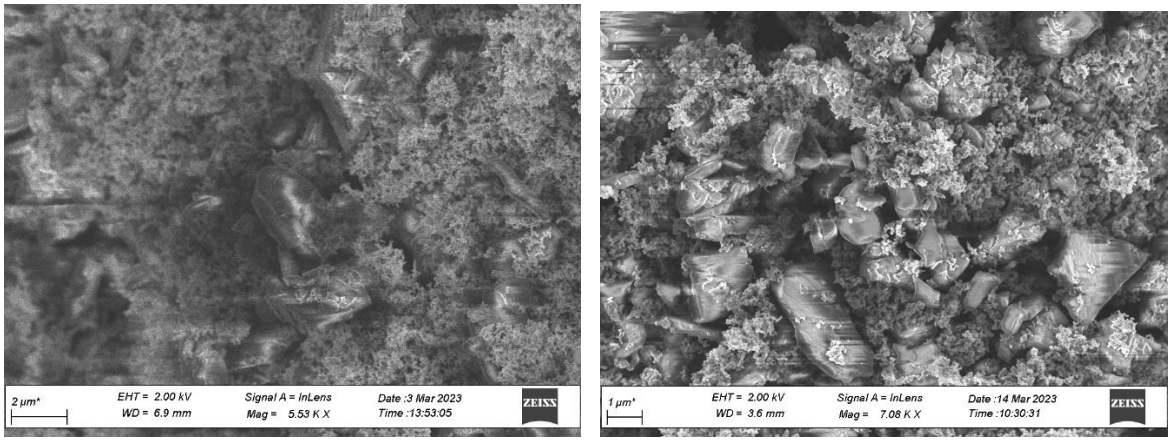

Fig. 21 SEM images of Li_4-*p*-DOBDA with ultrasonication, a.) NS sample (left) and b.) PS sample (right)

Their GCD also disappointingly achieve very low first cycle discharge capacity of 48.3 mAh/g (NS) and 45.2 mAh/g (PS), with observed rapid capacity fading. Although it achieves low polarization of 0.085 V and 0.114 V in the first cycle respectively, however it became significantly worse to 0.345 V and 0.332 V respectively, from the second cycle onward in fig. A3 in the appendix. The lower particle size in PS possibly contribute to lower polarization as there is increased contact surface area than NS sample. Based on this performance, this nanosheet route is deemed unsuitable for Li_4-*p*-DOBDA until further optimization will be taken to adjust and modify several parameters (such as the time of sonication and other cell optimization). Separate research on solubility of the compound at higher voltages is also needed. Furthermore, whenever the capacity is not limited for most profiles, it exceeds the theoretical capacity possible and makes an additional hump, which remains for further investigation (by ex-situ FTIR) to determine what soluble products or redox reaction happens between 3.7 – 3.9 V vs. Li^+/Li that contribute to rapid capacity degradation in subsequent cycles.

Even though nanoparticles reported by Jun Chen *et al*. paper performed slightly poorer than nanosheets on their chosen organic material, however it still outperformed the bulk particle

significantly [76]. In the next section, the ball-milling method will be discussed and how it affects the physical and chemical properties, as well as its electrochemical performance.

V.1.3.2 Ball-Milling

Ball milling works by utilizing the vibration of a pre-setup frequency to facilitate repeated grinding and collision between the materials for a specific duration, creating impact and attrition to reduce particle size as shown by fig. A4 in appendix [80]. Different balls with varying diameters can be used to control the final particle size. The particle size reduction depends on both the frequency and time applied during ball milling. The purpose of using ball milling is to make composite, where 3 different components (active material, conductive carbon and binder) are in contact with each other, ensuring uniformity throughout the sample regardless whichever part of the sample was taken. This is different from hand grinding, where the uniformity from the manual pressing is not likely to be guaranteed.

With higher frequency, there will be higher energy applied to the material, resulting in higher centrifugal force, which makes the resulting structure more uniform and yet also more amorphous, as well as increased contact area between particles due to a more compact structure, which reduces porosity. Conversely, lower energy applied means the mass of balls tend to slide or roll over each another, preserving more of the crystal structure compared to higher energy. However, due to less shaking, it tends to be less uniform in terms of particle size reduction and a less compact structure, means less porosity is reduced compared to higher energy. With longer milling time, more cycles occur that grind distinct areas of the sample, resulting in more uniform structure. Since it is important to have more crystalline structure for better electronic and ionic conduction, as well as optimized porosity for ion conduction as well, there exists an intermediate, optimized frequency and time to get the best structure. In this study, 5 Hz (low energy) and 25 Hz (high energy) will be applied and their differences will be compared for further investigation and optimization. At the critical speed, steel balls that mainly grind the particles will start to rotate along the cylindrical tube, which means no further grinding or particle size reduction occurs, so the determined frequency should not exceed nor drop far from this value.

There are several advantages in using ball milling method. Firstly, since it is contained in stainless steel jar, the purity can be maintained with minimum loss of materials. Secondly, the ball milling system requires minimal installation space and has lower maintenance costs. Thirdly, it is easily cleaned and consumes less energy. Finally, with various ball sizes, the capacity and fineness of the resulting particle can be tuned by adjusting the number and diameter of the balls. In addition, it is also suitable for both

dry and wet samples. However, it is not suitable for very large quantity of materials, as well as some sensitive matters where strong vibration needs to be avoided. Regular observations are also needed to avoid wear inside the cylinder seeps into the sample and contaminate the final product.

V.1.3.3 Composition with Graphene

Graphene is a 2D single layer compound of carbons, which is also a building block layer of graphite. Graphene is added because of its higher surface area/volume ratio, which means for the same surface area of contact it allows for a lower mass necessary, boosting the cell's specific capacity [81]. Besides that, graphene exhibits sp^2 hybridization, where each Carbon atoms connected to 3 other atoms in the 2D plane, leaving one free electron (π electron) that can be located below or above the graphene sheet. This configuration results in high electronic mobility, with mobility at low temperature reaching $2 * 10^5$ cm^2 V^{-1} s^{-1}, contributing to excellent electronic conduction, [81]. Furthermore, graphene possesses inherent characteristics such as high thermal conductivity, elasticity, hardness and flexibility which are desirable to enhance properties of the electrode materials in a battery as shown by fig. A8 in the appendix. Graphene has wide variety of applications due to its excellent properties but at the expense of higher cost, that's one of the reasons why it is only used as much as 10% in this experiment for the electrode composition. Moreover, graphene is also 5 times lighter than Aluminium, one of the lightest metals, which will boost the specific capacity and energy output of the cell [81]. Inclusion of graphene can aid on the polarization and solubility issue that will be shown on the post-cycled cell.

V.1.4 Physicochemical characterization of Li_4-*p*-DOBDA

V.1.4.1 Fourier Transform Infrared Spectroscopy of Li_4-*p*-DOBDA

Fourier Transform Infrared Spectroscopy (FTIR) is used to identify functional groups and molecular structure of compounds (or "fingerprint") by finding signatures of chemical bonds. The samples absorbed the IR radiation and convert it into characteristic stretching, rotational and \ vibrational mode (depending on geometry of the molecule) that can be detected in different wavenumber with varying intensities.

Fig. 22 shows the normalized peaks of FTIR Pattern of Li_4-*p*-DOBDA, its precursor ligand (H_4-*p*-DOBDA), as well as the 4 composite profiles. Based on the pattern above, Li_4-*p*-DOBDA is compared with its ligand H_4-*p*-DOBDA. The absence of phenolic bond (PhO-H, 3419 cm^{-1}) and carboxylic acid bond (COO-H, 2400-3100 cm^{-1}) in Li-containing patterns confirms the complete deprotonation of the ligand (left

figure). Moreover, in the right side of fig. 22, it also manifests the shift of peak of carbonyl (C=O) band, which is signature of carboxylate class at 1668 cm^{-1} that undergoes a significant bathochromic shift to 1574 cm^{-1}, as negative charge of the carboxylate reduces the vibration energy of the carbonyl bond. The presence of the enolate bond (C-OLi) at 1220 cm^{-1} indicates the successful lithiation process and absence of ligand in the final compound. Furthermore, the signature of C=C aromatic bonds in the range of 1550 cm^{-1} to 1375 cm^{-1} confirms the formation of Li_4-*p*-DOBDA molecule. Finally, the absence or negligible peaks around 1000 cm^{-1} indicates that the compound is pure and free of traces of methanol.

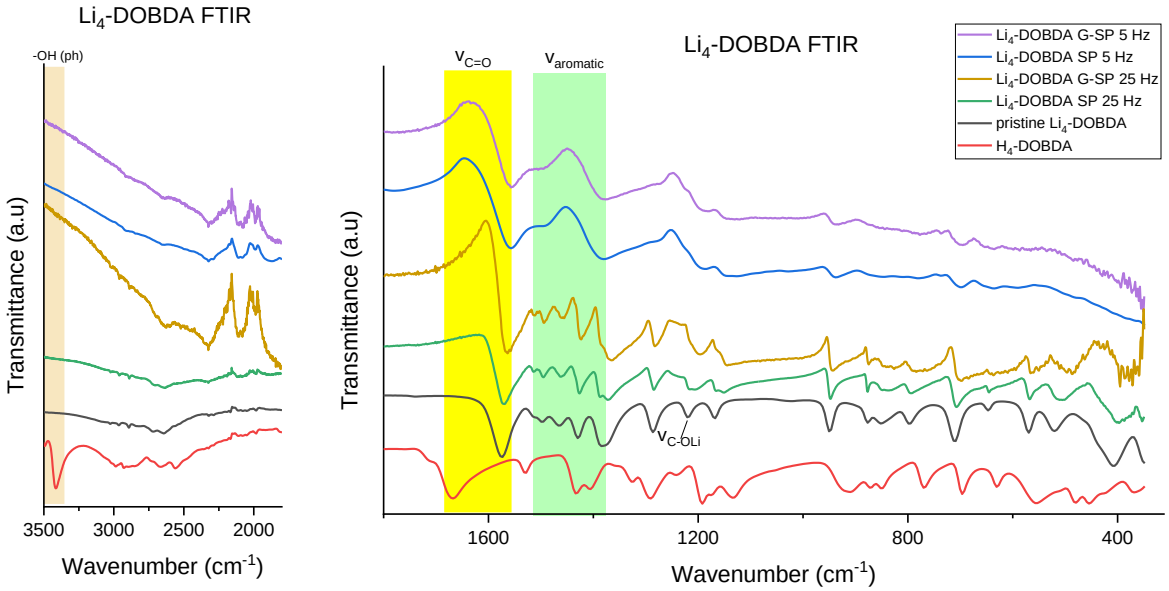

Fig. 22 FTIR Pattern of Li_4-*p*-DOBDA between 3500 cm^{-1} to 350 cm^{-1} wavenumbers

In comparison with the composite, the mechanochemical treatment of ball-milling does not affect the position of the major peaks. The peaks remain relatively unchanged, indicating that the compound is stable during the formation of the composite. It can be observed that the samples show similarities within the same frequency range of 5 Hz and 25 Hz, respectively, regardless whether graphene and SP altogether or SP are used as composites.

V.1.4.2 X-Ray Diffraction of Li_4-*p*-DOBDA

X-Ray Diffraction (XRD) is a technique used to analyse phase purity, crystallinity, size and strain of the sample. With higher crystallinity, the intensity of the diffracted peak increases due to constructive

interference, as the diffractions are in phase due to similar wavelengths according to Bragg's law [82]. This is the case for lower energy 5 Hz sample. However, in amorphous sample with higher energy vibration of 25 Hz, the diffractions occur in different wavelengths that are out of phase, cancelling or reducing the diffracted peaks' intensity due to destructive interference. The normalized peaks of pristine Li_4-*p*-DOBDA are compared with the simulated pattern, as well as the 4 profiles of the composite below in fig. 23.

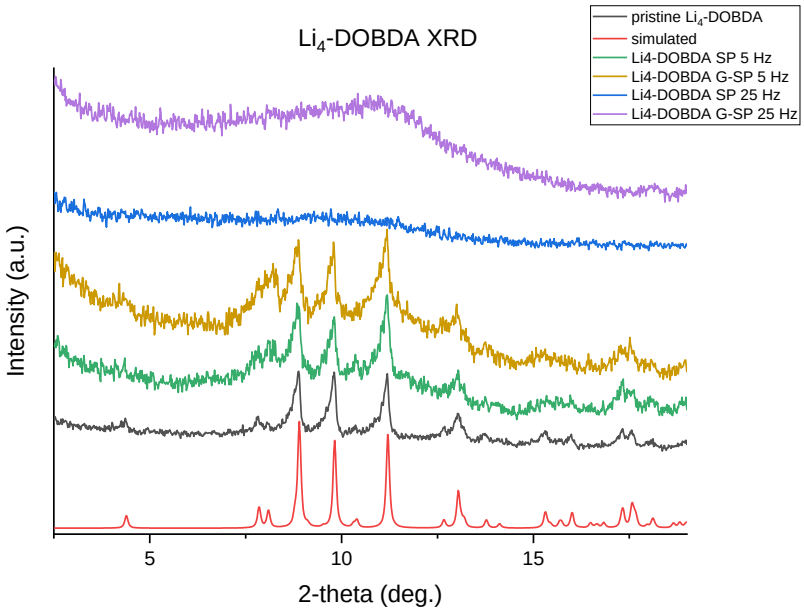

Fig. 23 XRD Pattern of Li_4-*p*-DOBDA and the Composites

XRD Pattern of pristine and composites are compared with simulated Li_4-*p*-DOBDA (fig. 23). The pristine Li_4-*p*-DOBDA shows good agreement with the simulated pattern of Li_4-*p*-DOBDA, suggesting the formation of the same phase. The diffraction peaks of Li_4-*p*-DOBDA at 4.4°, 7.88°, 8.9°, 9.8°, 11.2°, 13°, 15.3°, 17.6°, showing that the Lithiation is successful, which is also supported by FTIR pattern discussed previously. Furthermore, it is also observed that the higher intensity peaks of Li_4-*p*-DOBDA are preserved in 5 Hz composite of SP and G-SP, while the peaks disappear in 25 Hz composite of SP and G-SP. This shows that 5 Hz composites have higher crystallinity than 25 Hz composites as the higher energy in 25 Hz eliminates the diffraction peaks (loss of crystallinity), resulting in a very poor crystalline structure (amorphous). It can be inferred that the 25 Hz composites may have a smaller crystallite size than 5 Hz composites, conforming to the lower order of crystallinity. Furthermore, the observed peak broadening in 25 Hz composites may be attributed to disorder, which possibly cause greater micro-strains in the crystals. The strain and crystallite size can be calculated and analysed by Scherrer's equation [83].

Another possibility can be a smaller crystal formation, with presence of defects in the crystal. The difference between both 25 Hz composite is shown on the location of the 3 highest peaks, as for 25 Hz-SP has perfectly flat profile, while G-SP 25 Hz shows a broad hump, turning from 3 peaks into 1 broad, lower intensity peak. This can be an indication that G-SP 25 Hz shows slightly more crystalline (higher order of crystallinity) structure, even though both 25 Hz composite samples are amorphous in comparison to the pristine Li_4-*p*-DOBDA sample. Since the electrode needs certain amount of porosity to absorb the electrolyte, having more amorphous structure is not always a disadvantage, depending on how much fraction porosity is left, type of porosity and how it affects the ionic conduction. If the structure becomes more compact, it can be also detrimental to the ionic conduction despite the boost in mechanical strength and fracture toughness of the electrode. Overall, the diffractograms of pristine Li_4-*p*-DOBDA sample matches with the 5 Hz samples, since the 5 Hz ball milling process does not affect the phase and crystal structure. In contrast, 25 Hz composites are converted into lower crystalline phase (amorphous). However, similarity of 25 Hz composites FTIR with 5 Hz and pristine samples suggested that the local chemical structure remains the same as pristine, but with lower crystallinity order, which subsequently let 25 Hz SP and G-SP samples to become more amorphous in nature.

V.1.4.3 Scanning Electron Microscopy of Li_4-*p*-DOBDA

Scanning Electron Microscopy (SEM) characterization provides valuable insight about morphology and particle size of all the four profiles of combinations between ball-milled Li_4-*p*-DOBDA under 5 Hz and 25 Hz, both SP and SP with 10% Graphene samples. The morphology images are presented in fig. 24 and 25 below.

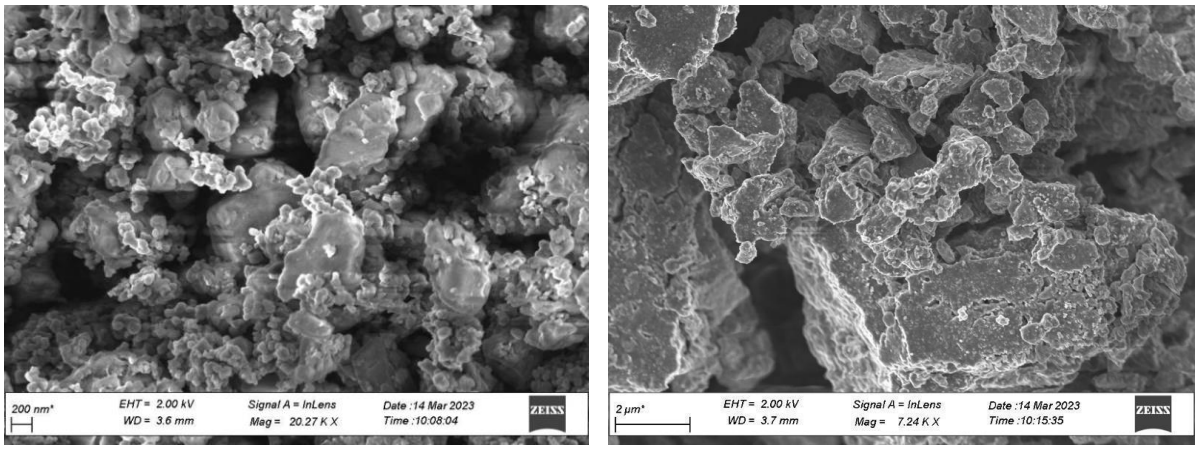

Fig.24 Image of Morphology and particle size of Li_4-*p*-DOBDA with SP, both 5 Hz (left) and 25 Hz (right)

These images reveal how the different energy of ball milling affects the morphology, particle size distribution and uniformity of the sample. Both samples have significant reduction in particle sizes compared to bulk and hand-grounded sample, which is the objective of the ball-milling process. Several particles in the images taken at random, are measured using ImageJ software, where the summary of results is described here. In the case of SP 5 Hz, the composite's particle size ranges between 430 nm to 1.07 μm with an average size of 736 nm and a standard deviation close to 300 nm. On the other hand, the SP 25 Hz's composite's particle size are very small that the size of the particles cannot be identified, but the agglomeration of nanosized particles, which can be perceived, spans between 850 nm to 1.27 μm with a mean size of around 1 μm and a standard deviation of less than 170 nm. It can be observed that 25 Hz sample appears to be more uniform than 5 Hz sample due to a narrower particle size distribution. It can also be seen that the different components in the composite mix more thoroughly in 25 Hz, more than 5 Hz, where some of the Carbons are still loosely detached from the active material. With higher reduction of particle size in 5 Hz than 25 Hz during each 15 minutes sessions, these findings suggest that there may be an optimized frequency and duration combination that achieves both significant particle size reduction (like in 5 Hz) and improved uniformity (like in 25 Hz), which can be investigated further beyond these preliminary findings.

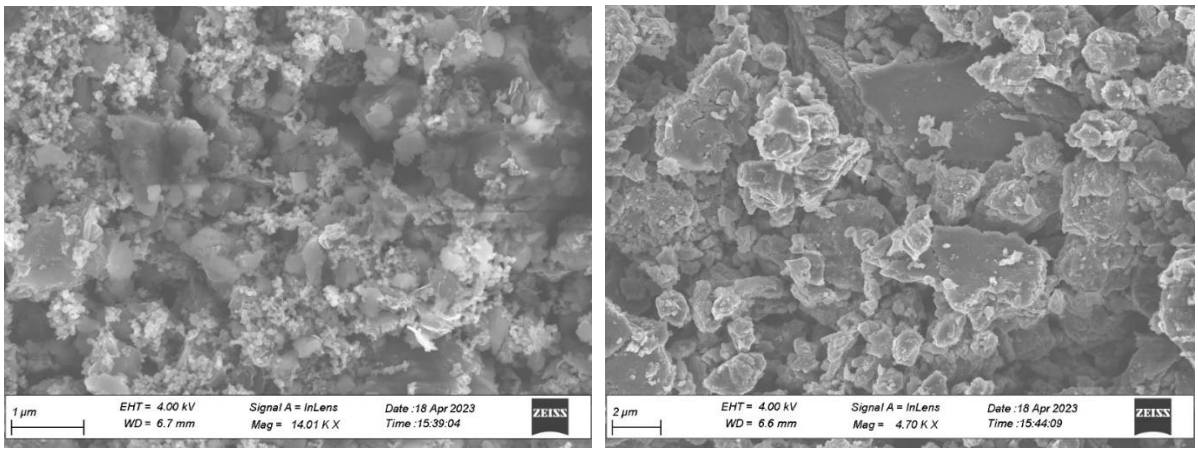

Fig.25 Image of Morphology and particle size of Li_4-*p*-DOBDA with SP and Graphene, both G-SP 5 Hz (left) and G-SP 25 Hz (right)

Similarly with the SP samples, both G-5 Hz and G-25 Hz samples have also achieved significant particle size reduction compared to the bulk, hand-ground and ultrasonicated samples. However, the mean

size and its standard deviation increases with an additional of graphene, which obviously has different size and orientation than SP carbon, compared to exclusively SP-composite samples. For G-SP 5 Hz, the composite's particle size ranges between 400 nm to 1.57 μm with average size close to 800 nm and standard deviation of 367 nm. In contrast, the G-SP 25 Hz's composite's particle size ranges between 819 nm to 2.06 μm with average size around 1.48 μm and standard deviation of 528 nm. In G-SP 25 Hz, the particles are observed to be agglomerated, making it challenging to precisely identify the particle sizes due to agglomeration of nanoparticles. Similar to the SP samples, the uniformity and mixing of 25 Hz samples are observed to be better than 5 Hz sample due to the presence of loose SP and graphene particles appear more separated from the active material in 5 Hz compared to the solid composite particle in 25 Hz. The pattern of improved uniformity and mixing of the composite components in 25 Hz samples compared to 5 Hz is observed consistently between both frequencies, regardless of the constituents.

It is evident that the 5 Hz particles undergo less particle size reduction, while the 25 Hz particles have smaller grain size, albeit with some agglomeration. This phenomenon may be attributed to more centrifugal forces that rotate with the ball mill rather than increased grinding between the particles. It can be noted that the critical frequency that switch from more grinding to more rotation phenomenon has likely been crossed, and the optimum frequency possibly lies between 5 to 25 Hz. However, the composite produced at 25 Hz displays more uniform mixing compared to the 5 Hz sample, as more energy and vibrations in 25 Hz facilitate more frequent particle grinding per second, resulting in a more solid appearance of the composite particles. The solid structure enhances electronic conduction by preventing carbon particles from being washed away or separated from the cathode during cycling by the electrolyte. Furthermore, longer ball-milling durations can ensure greater sample uniformity, particularly when employing lower energy frequencies. In addition, lower particle size can contribute to lesser polarization, but after a certain point can increase solubility and capacity fading too. Hence, the optimum particle size reduction and uniformity can be fine-tuned within the range of 5 to 25 Hz, and longer ball-milling durations beyond 15 minutes should be explored in further experiments.

V.1.5 Electrochemical Characterization of Li_4-*p*-DOBDA

V.1.5.1 Cell Construction

The electrochemical cell is constructed in a half-cell configuration with Li metal anode and organic Li_4-*p*-DOBDA cathode inside a coin cell, as described in the experimental methods section. It is designed

in such manner to test the capacity, polarization and cycling stability that are solely contributed by Li_4-*p*-DOBDA, without interference of contribution from other components, such as KB Carbon.

The chosen electrolyte is $LiPF_6$ in EC: DMC (1:1), as the $LiPF_6$ salt has intermediate average ion mobility and dissociation constant, which are optimized for its ionic conductivity. Since both properties have opposing trends, other electrolytes that have fast ion mobility (such as $LiBF_4$), have low dissociation constant, making the ionic concentration lower. Additionally, the choice of solvent mixture between EC: DEC is used to optimize the properties, as low viscosity and high dielectric constant is desirable. A low viscosity solvent like DMC is beneficial, as it reduces fluid resistance for the ionic transport, resulting in better ionic conduction due to inverse relationship between ionic mobility and viscosity, according to Stokes-Einstein's equation [84]. However, low viscosity solvent usually has low dielectric constant, which promotes ion-pairing as the critical interionic distance increases due to Bjerrum's relation, in which neutral ion pair doesn't contribute to ionic conduction, decreasing its useful carrier concentration [85]. Hence, high dielectric constant (with high viscosity) solvent like EC is also employed, to counteract the formation of ion pair, as the critical interionic distance decreases. Therefore EC: DMC (1:1) is chosen, which is also the most common electrolyte used for LIB. Additionally, a solubility test of 1-2 mg of Li_4-*p*-DOBDA in both electrolytes: $LiPF_6$ in EC: DMC (1:1) and LiTFSI in DOL/DME (1:1) for 17 hours shows no significant difference in solubility, as observed in their slightly differing shade of translucence, as shown in fig. A5 in the appendix.

Based on previous result by Louis *et al*. and previous section, and according to experimental procedure section, the electrochemical cell is limited in both potential range (2.7 – 3.9 V) and also its theoretical capacity (214.51 mAh/g). This limitation ensures that the first cycle does not exceed the theoretical capacity that had happened in numerous cells, which has been observed to lead a wide gap between the first and second cycle capacity, followed by subsequent rapid capacity fading, and also often accompanied by higher polarization. Going beyond 4V potential would risk the decomposition of the active material through the decarboxylation process, resulting in increased solubility or irregular behaviour that accelerates the capacity fading and polarization. The potential is cycled between 2.7-3.9 V, as this is similar to the potential range of some of commercial inorganic LIB, and it also aligns with average redox potential of 3.35 V, similar to LFP. If the limitation is too strict of going lower than 3.9 V, where stability is maintained, this will reduce the energy output as capacity and potential are reduced.

The limited capacity and potential cycling setup ensure the formation of Li reservoir on the cathode. Excess Li can be used to prolong the cycle lifetime, as efficiency gradually decreases and there will be less than 2 Li^+ and e^- exchange. Hence, this excess Li^+ from the reservoir can assist to decrease

polarization and sudden rapid capacity fading due to insufficient Li^+ for continuous ionic conduction, and still able to utilize number of electrons in redox process close to its previous cycle. For instance, 1.899 e^- is still utilized for 30th cycle compared to 1.9 e^- in its 29th cycle.

V.1.5.2 Galvanostatic Charge-Discharge of Li_4-*p*-DOBDA

Galvanostatic Charge-Discharge (GCD) measurement is utilized to characterize the electrochemical performance of the cell, as shown in fig. 26. The properties that can be discussed based on the graphs are its capacity, (redox) potential, polarization, Coulombic efficiency and cycling stability. The voltage vs. capacity curves on the (a.), (c.), (e.) and (g.) graphs show the evolution of how capacity changes with potential during cycling. The stability curves in (b.), (d.), (f.) and (h.) show the lithiation and delithiation process during charging and discharging over cycles, as well as the Coulombic efficiency of the redox process during intercalation/de-intercalation.

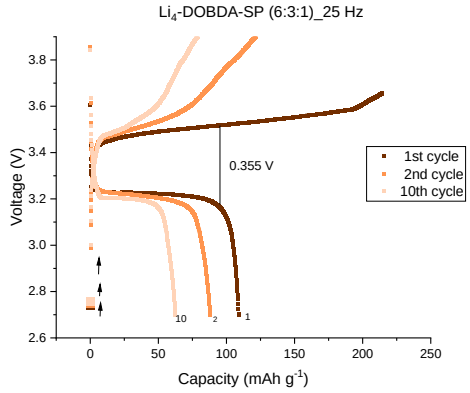

a.

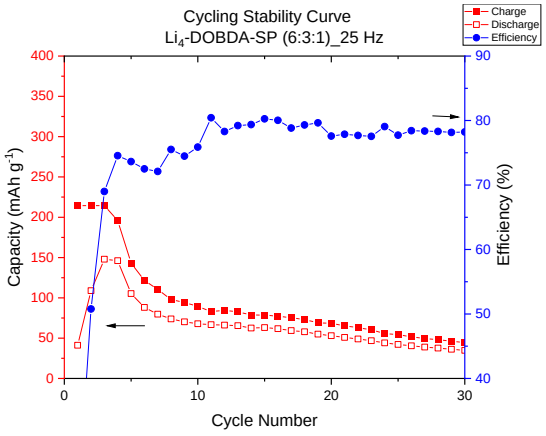

b.

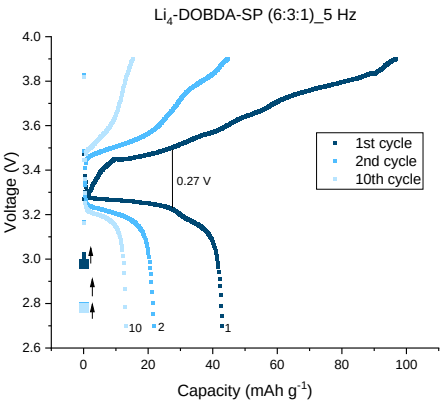

c.

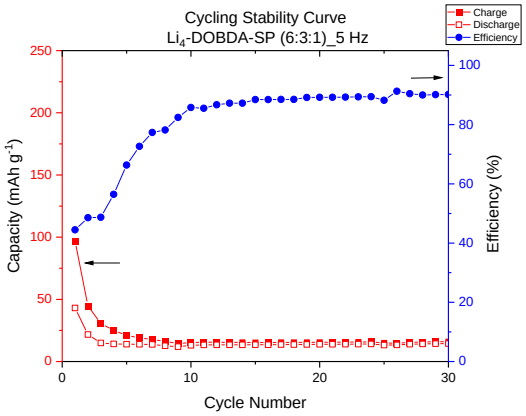

d.

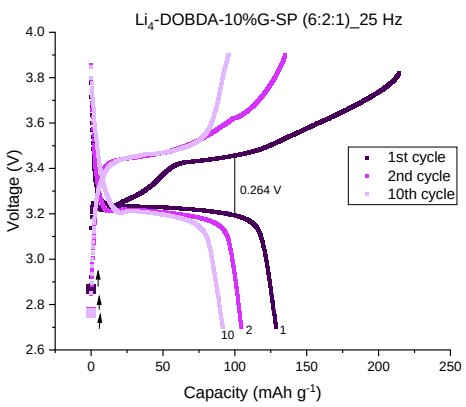

e.

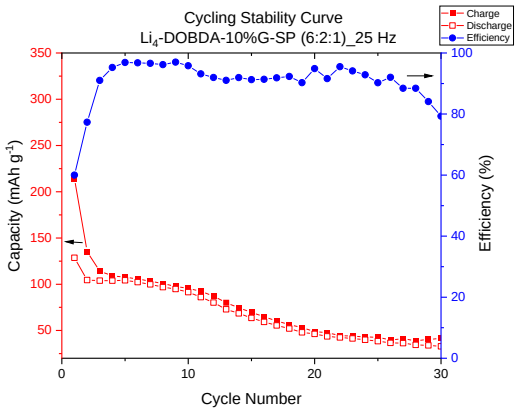

f.

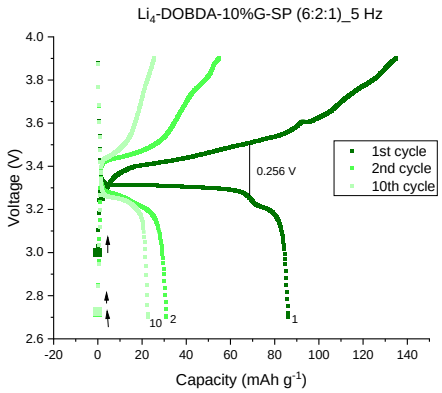

g.

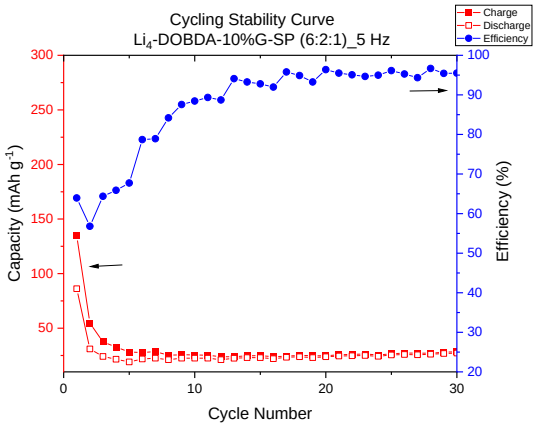

h.

Fig. 26 the GCD (left) and Cycling Stability curve (right) of a.) SP-25 Hz, b.) SP-5 Hz, c.) G-SP 25 Hz, d.) G-SP 5 Hz profiles, in order from top to bottom.

From the graphs, it can be observed that Li_4-*p*-DOBDA exhibit common issues related to polarization and solubility issues, that leads to capacity fading. All 4 profiles have achieved the objective of reducing polarization compared to the bulk or hand-grounded composite through downsizing particle size via ball-milling. The frequency of ball milling and the composition of the composite influence the shape of the GCD graph and its cycling stability. The solubility and capacity fading issue are more pronounced in the less uniform 5 Hz sample, as the capacity fading from 1st towards 2nd cycle are very significant (with wider gap) compared to 25 Hz samples. Nevertheless, the 5 Hz samples in the same category (with or without graphene) consistently exhibits lower polarization than the 25 Hz samples. This phenomenon correlates with the calculated Coulombic efficiency, which tends to be lower in 25 Hz. This is most likely due to the presence of more smaller particle sizes observed in 5 Hz. On the contrary, 25 Hz samples can reach its theoretical charging capacity on the first cycle and has more gradual capacity fading, indicating greater resistance to solubility issues, especially in the earlier

cycles. With high charge capacity, the 25 Hz samples also have higher first cycle discharge capacity than 5 Hz sample. All the profiles in capacity vs. voltage curve show plateau (where redox reaction occurs) at approximately 3.4 – 3.45 V, while the 25 Hz samples' profiles appear as separate redox steps due to flatter profile, behaving like a biphasic reaction, compared to 5 Hz samples' profiles that can be observed like a sloping line, that resembles more like solid solution reaction. The values from all 4 profiles on the graph are summarized on this table 2 below.

Table 2 GCD Intercalation Data of Li_4-*p*-DOBDA

ID	Name	First cycle Capacity (mAh/g)		Polarization (V)	10^{th} cycle Coulombic Efficiency (%)	10^{th} cycle Cycling Stability (%)
		Charge	Discharge			
1	Li_4-DOBDA SP (6:3:1) 25 Hz	214.41	108.87	0.355	79.37	57.38
2	Li_4-DOBDA SP (6:3:1) 5 Hz	96.73	43	0.27	85.81	30.42
3	Li_4-DOBDA 10%G-SP (6:2:1) 25 Hz	214.35	128.55	0.264	95.81	71.19
4	Li_4-DOBDA 10%G-SP (6:2:1) 5 Hz	134.76	86.15	0.256	88.44	26.23

Both 25 Hz samples reach theoretical charge capacity, but not in the case of 5 Hz samples. Interestingly, both 5 Hz samples in the same profile of SP or SP and Graphene profile outperforms the 25 Hz polarization by exhibiting lower values (0.085 V difference between SP only samples and 0.008 V difference between SP and graphene samples). Furthermore, it is revealed that SP-25 Hz has the second best first cycle capacity of 108.9 mAh/g, and also retains 57.4% capacity by its 10^{th} cycle, while also having the highest polarization value of 0.355 V. Moreover, SP 5 Hz consistently shows the bottom-tier performance of having the lowest first cycle capacity of 43 mAh/g, second lowest cycling stability of only 30.4% and second highest polarization of 0.27 V. These observed phenomena can be explained plausibly due to non-uniform mixing due to poor contact between the carbon particles and active material of the cathode in 5 Hz samples. However, it is interesting phenomenon that SP 5 Hz has almost 6.5% higher Coulombic efficiency than SP 25 Hz. In contrast, the nanosized composites of carbon and Li_4-p-DOBDA in the 25 Hz samples can improve the overall conductivity.

Moving on to graphene samples, G-SP 5 Hz exhibits the lowest polarization value of 0.256 V, but in the expense of being the second lowest in terms of first cycle capacity with 86.15 mAh/g, and also the

lowest capacity retention of 26.2% in the 10th cycle, despite boasting the second highest Coulombic efficiency of 88.4%. In contrast, G-SP 25 Hz demonstrates the best overall performance among all 4 profiles. It achieves the highest capacity of 128.55 mAh/g, showcases the second lowest polarization of 0.264 V with highest Coulombic efficiency of 95.8%, while its cycling stability remains uncontested compared to other profiles by retaining 71.2% of its capacity in the 10th cycle, as can be observed by more gradual capacity decays in the (e.) graph of fig. 26 compared to all other profiles. Both findings can be explained by the correlation between polarization and Coulombic efficiency. Higher polarization leads to decreased Coulombic efficiency and vice versa. SP 25 Hz and SP 5 Hz profiles exhibit the lowest and second lowest in terms of efficiency, respectively.

Overall, these results demonstrate the effectiveness of the ball-milling process in reducing polarization when particle size is reduced to the range of hundreds of nm to around 1 μm. Moreover, the higher energy 25 Hz ball-milling produces a more amorphous and uniform composite, resulting in improved first cycle capacity and cycling stability (slower capacity fading) compared to the 5 Hz samples. This may be attributed to reduced solubility or slower dissolution of the active material in the 25 Hz samples.

The addition of Graphene boosts the performance of the cell as a conductive carbon material, which outperforms the SP-only composite cells in terms of polarization and Coulombic efficiency, by narrowing the gap between charge and discharge. By replacing SP with an equivalent amount of 10% Graphene the composite benefits from graphene's lighter weight and higher surface area, facilitating greater contact between the conductive graphene and the active material. This improves the electronic conductivity and in turn, its specific capacity (specific measurement on these properties can be done as part of the perspective). It is interesting phenomenon with contrasting observation, that there is drastic improvement in Coulombic efficiency of almost 16.5% for 25 Hz samples, compared to only less than 3% increase in Coulombic efficiency for 5 Hz, when graphene is added. It can be concluded that graphene mitigates the solubility issue by exhibiting a higher first cycle capacity with less polarization, and greater cycling stability, as evidenced by less capacity fading (narrower gap) over cycles. The combination of both parameters' benefits gives rise to the overall best performance in G-SP 25 Hz sample among all profiles. In addition, the success of this method (which still holds potential for further optimization) paves the way for post-LIB technologies using respective DOBDA salt molecule as the cathode, warranting further research, as discussed in the next section.

V.2 Post-LIB DOBDA System

In this section, we will discuss the preliminary assessment of the material properties and electrochemical performance of Na_4-*p*-DOBDA and K_4-*p*-DOBDA as potential cathodes in post-LIB systems. For simplicity, the para position is assumed, and -*p*- notation will not be included for Na and K to simplify the writing. While Li_4-*p*-DOBDA has shown promising redox potential and specific capacity for LIB applications, the focus now shifts towards exploring alternative monovalent alkali systems such as Na and K. This assessment aims to understand the material properties and electrochemical behaviour of Na_4-DOBDA and K_4-DOBDA, considering their abundance compared to Li, which is becoming scarcer.

Although other ions like Na and K have lower redox potentials and generally lower specific capacities due to their heavier cations, their abundance can outweigh these limitations, especially in the context of diminishing lithium supply. This assessment will provide insights into the potential of these alternative systems for long-term sustainability. It is important to note that this discussion does not limit the implementation of post-LIB systems to monovalent alkali systems only. It can serve as a stepping stone for research and development in divalent alkali earth systems (e.g., Mg and Ca) or even transition metals (e.g., Zn), while adjusting the chemistry of each ionic system to uncover similar principles, preservation of the redox process in Li_4-*p*-DOBDA or observe new or exotic underlying redox phenomena, and optimize their respective systems. Hence, the next section will expound the preliminary assessment of the material properties and electrochemical performance of Na_4-DOBDA and K_4-DOBDA cathodes, keeping in mind that these systems are still far from being optimized.

V.2.1 Physicochemical characterization of Na_4-*p*-DOBDA and K_4-*p*-DOBDA

V.2.1.1 Fourier Transform Infrared Spectroscopy of post-LIB DOBDA

The FTIR analysis in fig. 27 shows comparison of various DOBDA salts molecules, Na_4-DOBDA and K_4-DOBDA (compared to its ligand H_4-*p*-DOBDA While Li_4-*p*-DOBDA and Na_4-DOBDA was successfully synthesized after drying under vacuum at 120^o C, K_4-DOBDA required drying under vacuum at 200^o C instead. Compared to Li_4-*p*-DOBDA, there's a shift of potential at 1220 cm^{-1} showing the signature of enolate bond C-OLi to C-ONa at 1209 cm^{-1} and C-OK bond at 1213 cm^{-1}, respectively. This shift confirms the success formation of Na_4-DOBDA and K_4-DOBDA (although purity level of K_4-DOBDA is unknown).

Another observed similarity is the bathochromic shift that occurs in Li_4-*p*-DOBDA, due to reduction of vibration energy of carbonyl bond caused by negative charge in carboxylate, also shift the Na_4-DOBDA

and K_4-DOBDA peaks as well. The shift of carbonyl bond vibration from 1668 cm^{-1} in ligand H_4-*p*-DOBDA are shifted to lower energy with higher wavenumbers 1594 cm^{-1} and 1590 cm^{-1} for Na_4-DOBDA and K_4-DOBDA, respectively, due to the size difference and distinct vibration energy. Finally, the major peaks of C=C aromatic bonds are also observed between 1550 cm^{-1} to 1375 cm^{-1} similar to Li_4-*p*-DOBDA, with slight shifting within the region, which further proves the formation of intended compounds, similar to Li_4-*p*-DOBDA. In addition, the absence of phenolic bond at around 3500-3600 cm^{-1} and carboxylic bond at similar wavenumbers in Li_4-*p*-DOBDA, as discussed in the FTIR section of Li_4-*p*-DOBDA, also confirms complete deprotonation of the ligand of H_4-*p*-DOBDA in forming the final compound, consistent with the expected result.

Both Li and Na salts have shown to have negligible to no trace of methanol between 1000-1050 cm^{-1} that are easily removed at 120° C, but K_4-DOBDA still has some trace of methanol, that indicates higher affinity of bonding (due to larger coordination number of K) to methanol compared to Li and Na's counterparts, which makes it more difficult to remove even at higher temperature of 200° C. This is also tricky as drying further in vacuum at 250° C proves to be detrimental to K_4-DOBDA as colour changed from beige/creamy white to dark grey-brown that suggests possible deterioration and irreversible structural transformation that may decrease its electrochemical performance. Hence, K_4-DOBDA cell was not tested until the issue of trace methanol and the high energy binding with the hydroxide functional group could be resolved through further optimization.

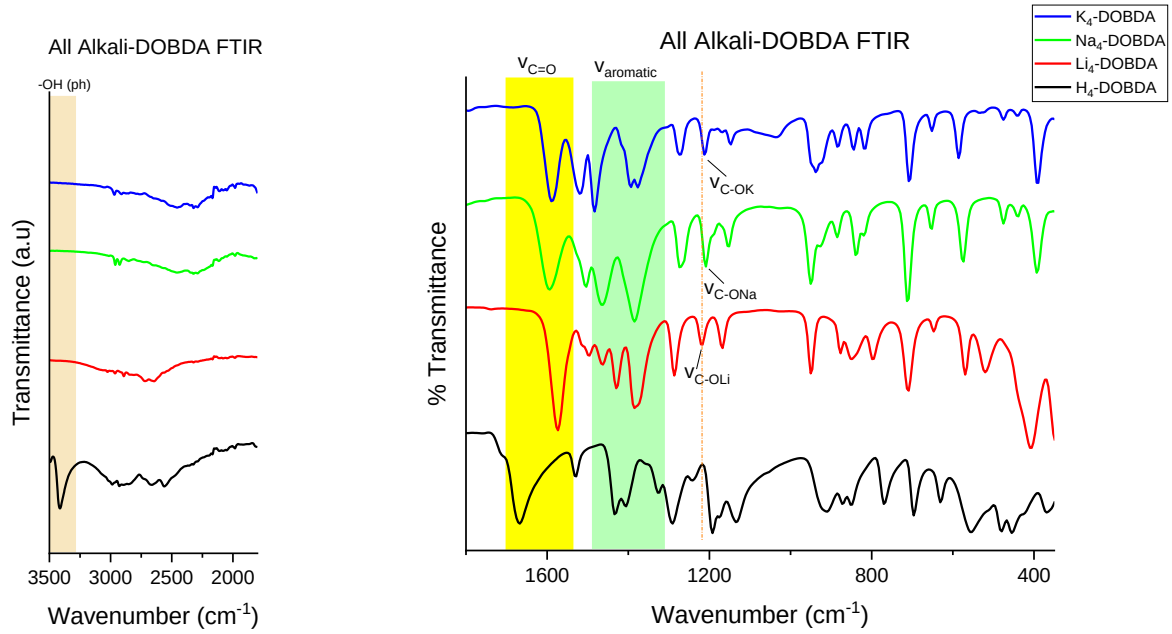

Fig. 27 Comparison of FTIR between DOBDA molecules of Li, Na and K in comparison to the ligand H_4-*p*-DOBDA

In comparison with their respective composites, as shown by fig. A7 in the appendix, FTIR of their composite shows similar positions of the peak with respect to their pristine counterparts. This indicates that the mechanical hand-grinding process does not affect the chemical composition or induce any irreversible structural transformation in the stable composite materials, which mechanochemical stability phenomenon is similar to Li_4-*p*-DOBDA discussed previously.

V.2.1.2 X-Ray Diffraction of post-LIB DOBDA

The XRD graph presented in fig. 28 below compares the diffractograms of DOBDA salts between simulated Li, Li, Na and K salts. The pattern of Li_4-*p*-DOBDA, Na_4-DOBDA and K_4-DOBDA exhibit slight differences from each other. However, the low angle peak of Li_4-*p*-DOBDA is located at approximately 4.5° 2θ, which is also present in Na_4-DOBDA and K_4-DOBDA, suggesting that the structures of these salts are somewhat similar. However, the coordination environment may differ among Li, Na and K, due to their respective coordination numbers of 4, 6 and 6 or 8. Consequently, this leads to slight structural variations between the salts.

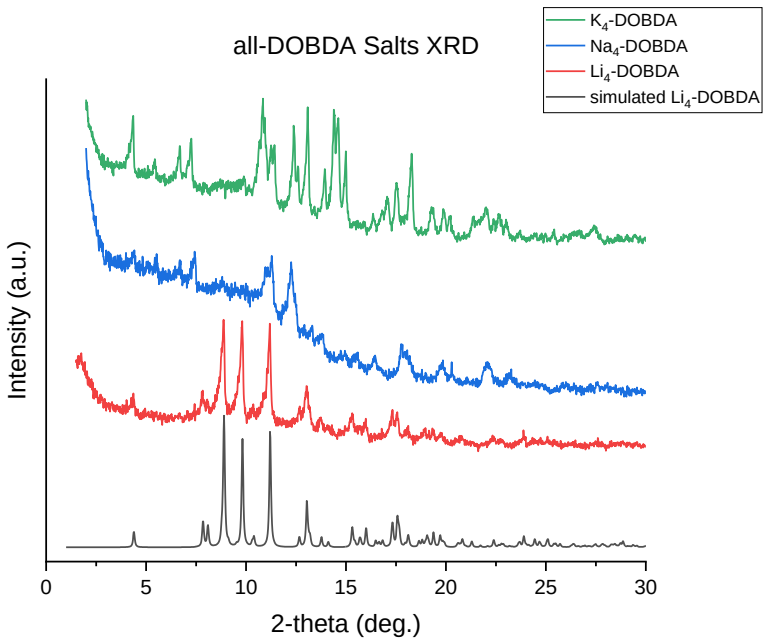

Fig. 28 XRD of all DOBDA salts

The sharpness and intensity of the peaks provide further insights. Na_4-DOBDA exhibits broader peaks compared to the other salts, indicating poorer crystallinity compared to Li_4-*p*-DOBDA and K_4-DOBDA. Additionally, Na_4-DOBDA displays noticeable peak shifts from 7.8° in Li_4-*p*-DOBDA to 7.45°. Besides that, the 3 intense peaks in Li_4-*p*-DOBDA at 8.9°, 9.8° and 11.2° have been reduced to only 2 peaks that have shifted to 11.3° and 12.3°. Another peak has also shifted from 17.3° in Li salt to 17.8° in this Na salt. However, the overall trend of rising and decreasing intensity patterns resemble those observed in Li, except for the observed shifts. Generally, the XRD analysis reveals peak broadening, with smaller crystallite size and fewer peaks with lower intensities in Na salt compared to Li.

However, K_4-DOBDA not only exhibits major peak shifts, but also dissimilar shape and sharpness of certain peaks compared to the Li and Na salt. K_4-DOBDA shows additional peaks at 6.7°, 11.4°, 12.4°, 14.4°, 15°, 17.1° and 17.6°, which are not observed in Li and Na compounds. Furthermore, there are shifting peaks in K_4-DOBDA compared to Li_4-*p*-DOBDA from 4.37° to 4.33°, 7.8° to 7.25°, 11.2° to 10.84°, 13.1° to 13.96°, 17.6° to 18.3°. The appearance of extra peaks and shift in peak positions can be interpreted as presence of trace Methanol that gets bonded with K_4-DOBDA, as analysed previously by FTIR. The higher coordination number of K with the methanol solvent makes it more challenging to fully remove the methanol from the sample, even after drying at 200° C.

By comparing the peaks' positions and the shifting peaks of Na and K salt compared to Li salt, in which Li_4-*p*-DOBDA has monoclinic crystal structure (in table A1 at appendix), it can be inferred that each salt possibly has a different crystal structure from one another. However, since the ligand H_4-*p*-DOBDA also possesses monoclinic structure with differing lattice parameters (a, b, c) and angle β, they are more likely to also have similar monoclinic structure, with distinct lattice parameters and angle from each other. The shift in the peaks, different values of Full Width at Half Maximum (FWHM), and variations in the crystallite size can be further determined using techniques such as Pair Distribution Function and Rietveld Refinement to obtain the precise values and characterize the crystal structures accurately.

V.2.1.3 Scanning Electron Microscopy of post-LIB DOBDA

V.2.1.3.1 Na_4-*p*-DOBDA

The morphology of pristine and SP composite of Na_4-DOBDA is shown on fig. 29. It has shown diverse range of particle sizes with a "rocky" morphology in the pristine sample. In the SP composite of Na_4-DOBDA, hand-grinding has reduced the particle size, but the particles are still far from being uniform, as the Carbon seems to be predominantly located around the electrode rather than being well-mixed with the electrode material, similar to the hand-ground Li_4-*p*-DOBDA sample discussed earlier. For pristine Na_4-DOBDA, the composite's particle size ranges between 1.5 μm to 6.4 μm with average size of 3.05 μm and standard deviation of approximately 1.6 μm. Comparatively, the particle size of the SP composite of Na_4-DOBDA varies from 788 nm to 2.96 μm with average size of 1.58 μm and a standard deviation of around 0.88 μm. Even though hand-grinding has reduced the particle size, however there is still room for improvement, as particle size reduction achieved by ball-milling in Li_4-*p*-DOBDA has shown beneficial effects on lowered polarization and solubility that can be applied here as well. Thus, further optimization can be pursued for the Na_4-DOBDA electrode, and the scientific knowledge gained is also transferrable to other Alkali and Alkali Earth systems.

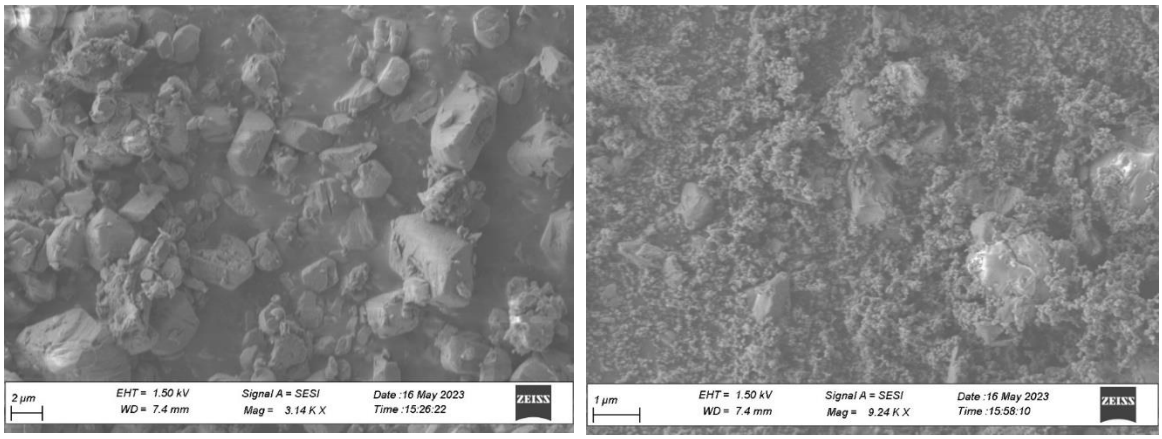

Fig. 29 SEM of pristine Na_4-DOBDA (left) and its SP composite (right)

V.2.1.3.2 K_4-*p*-DOBDA

Morphology of K_4-DOBDA is observed on fig. 30 below, displays "broken plate" morphology for the pristine sample. For both samples, distinct particle sizes resembling "plates" can be observed, which appear to be less uniform than in Na's and Li's counterparts. The hand-ground SP composite of K_4-

DOBDA is merely “blanketed” with Carbon, indicating a lack of uniformity in the composite formation, as the active material looks to be somewhat separated from the carbon. The particle size of pristine K_4-DOBDA ranges from 1.5 μm to 5.1 μm with an average size of 3.58 μm and a standard deviation of approximately 1.46 μm. Comparatively, the particle size of the SP composite of K_4-DOBDA varies between 1.3 μm to 4.08 μm with an average size of 2.63 μm and a standard deviation of around 1.22 μm. The ascending order of particle size for the pristine DOBDA particles is: Li < Na < K, which aligns with the pattern of increasing atomic radius and atomic weight. Nevertheless, improvement to reduce particle size, such as with ball-milling, which reduces polarization and solubility in Li_4-*p*-DOBDA cell can be implemented here for K_4-DOBDA, particularly if the purity of the sample can be ensured without any trace of Methanol (or at negligible levels).

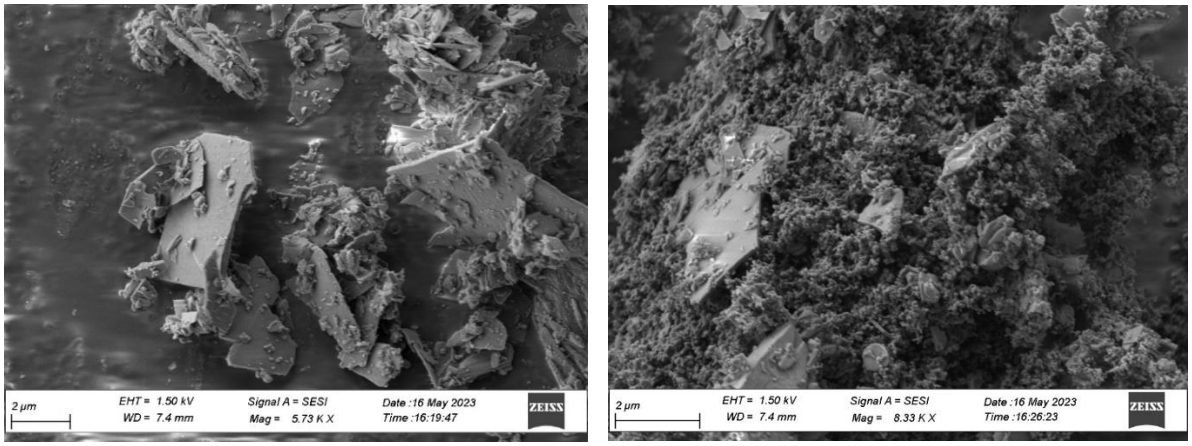

Fig. 30 SEM of pristine K_4-DOBDA (left) and its SP composite (right)

V.2.2 Electrochemical Characterization of Na_4-*p*-DOBDA

Na_4-DOBDA, due to its larger and heavier Na^+ cation than Li, has smaller theoretical capacity of 85.34 mAh/g, or only 39.8% theoretical capacity of Li_4-*p*-DOBDA. Hence, the expected capacity and energy output for Na_4-DOBDA is smaller than Li_4-*p*-DOBDA. However, the abundance of Na is around 1000x more than Li, which justifies the capacity difference worth it and highlights the potential for optimization. In the preliminary assessment conducted by Louis Sieuw, the electrode composite was evaluated using KB carbon to assess the initial performance before optimizing it in the SP composite, as shown in the GCD and cycling stability curve below in fig. 31.

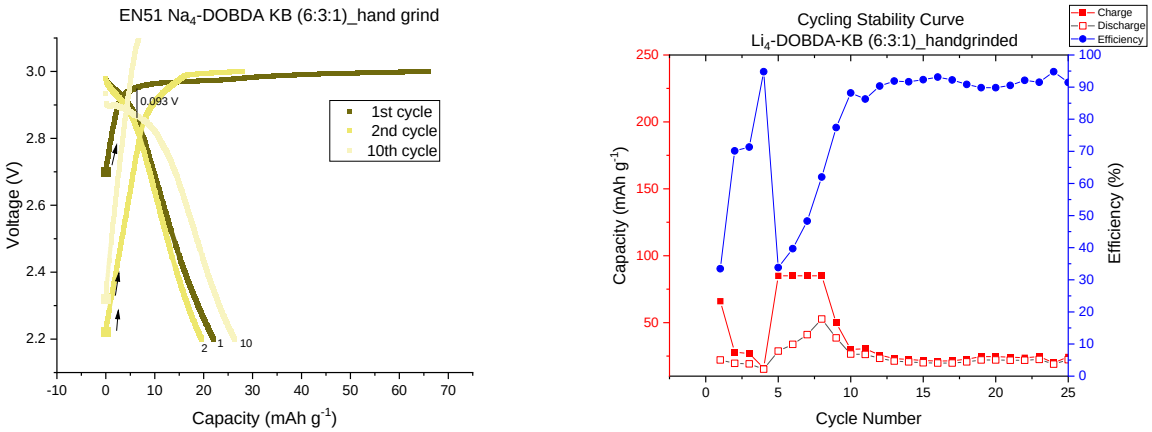

Fig. 31 GCD (left) and Cycling Stability Curve (right) of Na_4-DOBDA KB Composite

Na_4-DOBDA shows lower redox potential than its Li counterparts by exhibiting a plateau at around 2.95 – 3 V vs. Na^+/Na. When using a hand-grounded electrode, It demonstrates a first cycle capacity of 22 mAh/g and a tenth cycle capacity of 26.4 mAh/g, which corresponds to roughly a quarter to 30% of its theoretical capacity. The lower capacity can also be attributed to the higher average grain size of Na_4-DOBDA composite with respect to the Li_4-*p*-DOBDA composite. It shows gradual capacity degradation over time, indicating its resistance to solubility against the electrolyte, which is 1M $NaPF_6$ in EC: DEC (1:1). Furthermore, it has lower polarization of only 0.093 V, even though the polarization increases in subsequent cycles. This can be related to its Coulombic efficiency that reaches up to 94.8% available. This shows that Na_4-DOBDA has significant potential for improvement by further reducing particle size (using ball-milling) and investigating the chemistry in more detailed manner.

Based on experimental observation, since Na counter electrode for hall-cell configuration is prepared by cutting and rolling the Na into a thin anode, it could be argued that the variation in thickness and uniformity in preparing the Na anode may affect the overall weight and capacity of the cell, as well as the ionic transport during the redox process. Due to time constraints, Na_4-DOBDA SP composite (hand-grounded) is currently undergoing further optimization, as it has exhibited very little capacity (less than 10 mAh/g for its first cycle capacity) for meaningful investigation of the underlying phenomenon. Once optimized, the SP composite will also be ball-milled to further reduce polarization and improving capacity and cycling stability.

In this preliminary assessment, it is observed that the redox phenomena for Na_4-DOBDA is similar to Li_4-*p*-DOBDA, except that it's cycled between lower potential of 2.2 V – 3 V with limited theoretical capacity of Na_4-DOBDA as shown on the experimental section. The start contrast of the redox

phenomena is signified in Na_4-DOBDA by only showing 1 plateau that belongs to one-electron redox process instead of two-electron redox observed in Li_4-*p*-DOBDA. This difference can be attributed to higher coordination number of 6 in Na compared to 4 in Li during solvation in electrolyte. This leads to higher energy requirement during desolvation process, which in turn needs larger space that will exfoliate the electrode more easily, reducing the capacity even faster (and more rapid capacity fading) than in Li_4-*p*-DOBDA. Since K_4-DOBDA has larger coordination number of 6 or 8, then most likely K_4-DOBDA is predicted to show also only one-electron redox plateau like Na_4-DOBDA, most likely at different potential values than what's shown on the GCD of Li_4-*p*-DOBDA and Na_4-DOBDA. In addition, slower diffusion kinetics due to the larger ionic size of Na compared to Li also contributes to lower capacity, this can be tested further using Electrochemical Impedance Spectroscopy to verify these findings. Finally, optimization of alkalisation procedure needs to be verified and investigated further in more detail, considering slightly different chemistry involved.

The optimization Na_4-DOBDA still holds potential for further improvement. Despite its lower capacity and redox potential compared to Li_4-*p*-DOBDA, Na_4-DOBDA exhibits lower initial polarization, and also slower capacity decay with a hand-grounded electrode (as opposed to Li_4-*p*-DOBDA KB hand-grounded composite). This suggests that ball-milled nanoparticle of Na_4-DOBDA may exhibit even better performance in terms of lower polarization and solubility compared to Li_4-*p*-DOBDA, resulting in longer and better cycling stability, in expense of its lower capacity and potential, i.e., energy output. These characteristics could be valuable in markets where energy output is not the primary concern, whereas long-term stability and cycle lifetime are of greater importance. Similar trends can be expected for K_4-DOBDA and extended to other post LIB systems, with distinct redox potential, capacity and cycling stability values.

VI. Conclusion and Outlook

Li_4-*p*-DOBDA has shown to be a highly promising organic cathode for future organic batteries, owing to its favourable redox potential of 3.35 V, which is also air-stable. This redox potential is achieved through the combined effects of through-space charge modulation that creates higher repulsion and boost its redox potential, in conjunction of the through-bond effect. Furthermore, Li_4-*p*-DOBDA also exhibits a high specific capacity, similar to other benzoquinone molecules, further highlighting its potential as a viable organic cathode for future applications. Li_4-*p*-DOBDA was successfully synthesized under inert atmosphere using Schlenk tube technique. However, similar to other organic molecules, solubility and polarization issue are the main challenges when it comes to practical implementation and scalability for commercial battery production. To overcome these challenges, ball-milling technique were employed to reduce the particle size of Li_4-*p*-DOBDA. Additionally, optimization have been undertaken to fine-tune the material properties and improve the overall electrochemical performance of Li_4-*p*-DOBDA.

The synthesized Li_4-*p*-DOBDA was found to be pure and free of excess trace methanol solvent. The characteristic peaks observed in the FTIR spectrum were consistent with the expected signature of the bonds, which are in agreement for the ligand H_4-*p*-DOBDA, as well as the enolate CO-Li bond. Mechanochemical treatment using ball-milling did not alter the key signature peaks, showing the stability of Li_4-*p*-DOBDA composite. XRD analysis revealed that the peaks of the more crystalline 5 Hz samples matched those of the pristine Li_4-*p*-DOBDA, suggesting the preservation of its crystalline structure. On the other hand, the peaks of the 25 Hz samples showed broadening or disappearance, indicating a more amorphous structure, with very low crystalline order. SEM analysis further confirmed that the particle size of pristine material was reduced to a range of 400 nm to 2 μm through ball-milling. This reduction in particle size contributed to lower polarization, reduced solubility, and slower capacity fading. Particle size in 25 Hz samples appear to be more uniform with a lower standard deviation, and the active material was observed to more evenly mixed with the SP/graphene conducting carbon and PTFE binder.

The addition of graphene had a positive impact on increased electronic conductivity (that can be further measured by Electrochemical Impedance Spectroscopy for precise value), surface area and specific capacity. This resulted in further reduction of polarization and solubility, while amplifying the initial capacity. Among the four profiles studied, the best electrochemical performance profile was obtained for the G-SP 25 Hz composition, which contained 10% graphene that was added to the SP composite (forming this composition: 60% Li_4-*p*-DOBDA, 20% SP Carbon, 10% Graphene and 10% PTFE). By employing high energy 25 Hz ball milling to this particular profile, this composition exhibited

the highest first cycle discharge capacity of 128.6 mAh/g, with 91.5 mAh/g or 71.2% capacity was retained on its 10th cycle, along with 95.8% Coulombic efficiency, as well as a reduced polarization of 0.264 V. Both adjustments resulted in a 0.207 V lower polarization, representing a 44% reduction compared to the hand-grounded KB composite, which was originally done on Louis' thesis. In contrast, SP 5 Hz profile has achieved the worst performance with the lowest first cycle discharge capacity of 43 mAh/g, with 13.1 mAh/g or 30.4% capacity was retained on its 10th cycle, along with 85.8% Coulombic efficiency, as well as a second highest polarization value of 0.27 V among all 4 profiles. These findings also prove the effectiveness of reducing the composite into nanoparticle size using ball-milling, as it increases the contact and surface area, with 25 Hz ball-mill had a greater effect compared to 5 Hz mode. Moreover, the incorporation of graphene enhanced its electronic conductivity, higher surface area and better specific capacity, surpassing the performance when only SP carbon used as sole conducting carbon in the composite.

Finally, DOBDA molecule was deemed suitable and promising to be transferred as organic cathode in any post LIB system. By investigating new chemistry and optimization processes, the DOBDA molecule can be transferred as an organic cathode with different cations such as Na, K, Mg and Ca. This is driven by the higher abundance of these elements and the need for sustainability, considering the exponential increase in demand for Li (with decreasing supply) in various applications, mainly EVs, electronics and renewable energy.

Preliminary assessment showed that Na_4-DOBDA and K_4-DOBDA were successfully synthesized. However, FTIR and XRD analysis revealed that only Na_4-DOBDA exhibited a pure compound as K_4-DOBDA had exhibited stronger bonding with the solvent Methanol, which were not fully removed from K_4-DOBDA structure upon drying under vacuum at 200^o C. This can be attributed to the higher coordination number of 6 or 8 for K compared to 6 for Na respectively, which leads to increased solvation between the active material with the solvent. It is highly likely that all the compounds show monoclinic crystal structure with varying lattice parameters and angles), as observed from the shifting positions of major peaks in both FTIR and XRD analysis. Both Na and K salts displayed average particle size larger compared to the Li salt using SEM.

Furthermore, Na_4-DOBDA with a hand-grounded KB composite was tested and showed a first cycle discharge capacity of approximately 30.9% of its theoretical capacity, which was 26.4 mAh/g in this case. In addition, it can be inferred that due to only 1 redox plateau observed, they are likely to have only one-electron redox process as opposed to two-electron redox in Li_4-*p*-DOBDA, with lower redox potential (2.95 V for Na) and initial first cycle capacity. The lower starting polarization of 93 mV, which definitely can be lowered with ball-milling, are attractive for achieving high stability and longer cycle

cells, in particular for Na, especially with the rise of SIB as an alternative potential for LIB. These findings can also be extended for K, Mg, Ca cells with similar DOBDA system available.

There are indeed several possibilities to optimize the DOBDA system further and address the challenges associated with polarization, solubility and stability. Firstly, on functional group tuning. Since Li_4-*p*-DOBDA has shown higher potential with through-space electronic effect, it is possible to explore the modification of suitable functional group and their positions (ortho, para) and leverage through-space electronic effects as well. This can boost redox potential (widening the potential window) and mitigate polarization and solubility issues for better stability. Systematic modifications can be performed to identify the optimum functional group configurations (balance between EDG and EWG substituents, as compromise between less solubility vs. higher redox potential, respectively). Regarding the formation of hump/kink at higher voltage when cycled beyond 3.9 V or when the capacity is not limited, it will be interesting to characterize this with ex-situ FTIR to find out the nature, chemistry and solubility issue of this soluble oxidized compound due to decarboxylation further. In addition, the electronic conductivity with or without graphene can be measured from Impedance Measurement using EIS, to calculate the exact gain of electronic conductivity when 10% graphene is added.

Secondly, ball milling parameter combination of both frequency (Hz) and time (s) can be optimized even further to achieve the desired morphology and particle size range. Fine-tuning these parameters can lead to improved performance and better control over the properties of the DOBDA composite. Thirdly, when Metal-Organic Framework (MOF) and/or Coordination Polymer are employed, it will reduce the solubility issues by providing a more stable and robust backbone that interacts with the electrolyte. This enhances the overall stability and lifespan of the battery. Besides that, replacing the glass fibre separator with an Al_2O_3 ceramic-coated separator can further mitigate the solubility issues.

Fourthly, by transitioning from a liquid electrolyte to a solid-state electrolyte, this solution can completely eliminate solubility issue as the battery turns into all-solid-state battery. However, this comes at the expense of slower ionic conductivity through solid-state electrolyte (which is usually ceramic, polymers or hybrid-based). When polymer electrolyte is used, then it paves the way for all-organic battery, as there are more ONEMs discovered as anode, due to much lower redox potentials. Another option is on ceramic/inorganic-based electrolyte, such as halide-based Li_3InCl_6, which exhibit stability up to 4V (that is close with the upper limit of testing potential range in the experiment), which further expands it capacity further. Finally, when the system is optimized, anode-free battery configuration can be considered. This eliminates the anode mass, boosting its specific capacity. In

addition, it addresses safety concerns associated with Li metal dendrite formation, which is swiftly eliminated.

Overall, by incorporating these optimization strategies, the DOBDA system can be further enhanced and transferred to post-LIB system for optimization further, as it leverages on similar mechanism and observed redox phenomena from R&D progress in Li_4-*p*-DOBDA.

VII. Appendix

Commercial Ligand H_4-*p*-DOBDA used:

Fig. A1 H_4-*p*-DOBDA from Sigma-Aldrich

Air stability of Li_4-*p*-DOBDA synthesized under ambient air and Schlenk tube method

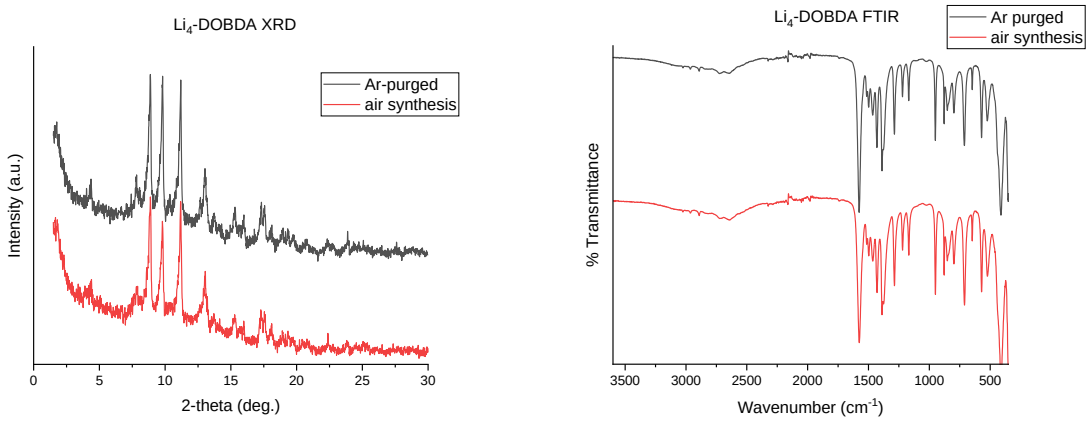

Fig. A2 XRD pattern of air-synthesized and Ar-purged Li_4-*p*-DOBDA (left) and FTIR spectra of both synthesis methods of Li_4-*p*-DOBDA (right)

GCD of NS and PS samples of Li_4-*p*-DOBDA through ultrasonication process:

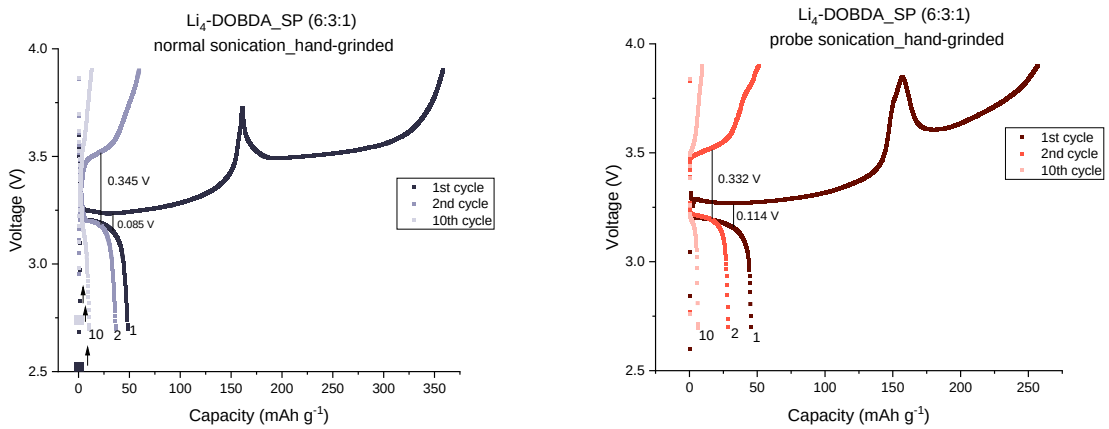

Fig. A3 GCD of NS and PS samples

Ball-milling Equipment and Components:

Fig. A4 Stainless steel jars and equipment for Ball Milling (There is equivalent number of balls to make identical weight, only 1 jar is shown with ball)

Electrode Solubility Test in 2 Distinct Electrolytes:

Fig. A5 Solubility Test of Li_4-*p*-DOBDA in 1M $LiPF_6$ in EC: DMC (1:1) and 1M LiTFSI in DOL/DME after 17 hours

Formula	$C_{10}Li_4O_6$ (6 H atoms not included)
Powder data	
Powder Data temperature (K)	295
M_r	243.86 (6H-atoms not included)
crystal system	Monoclinic
space group	$P2_1$
a (Å)	12.581
b (Å)	5.0934
c (Å)	9.5012
β *(deg.)*	124.4986 °
V (Å^3)	501.298
D_x (g cm^{-3})	1.616
Data collection	
λ (Å)	0.69425
θ_{min}–θ_{max} (deg.)	0.0044-29.7231
2θ step (deg.)	0.0089
Refinement	
Profile function	Pseudo-Voigt
R_p	5.19
R_{wp}	7.40

Table A1 Powder Data, Collection Data and Structure Refinement Parameters of Li_4-*p*-DOBDA

Cycling stability of Li_4-*p*-DOBDA KB and SP (initial composite in Louis Sieuw' thesis)

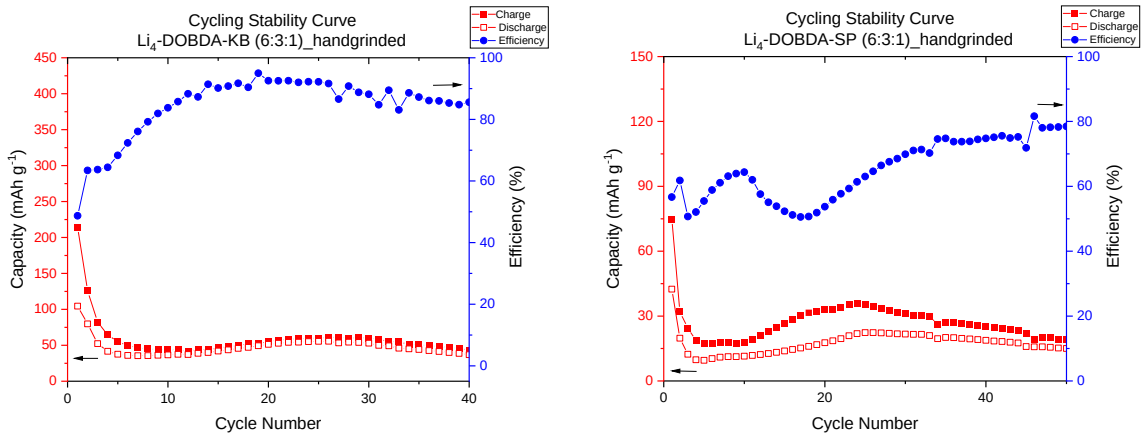

Fig. A6 Cycling Stability curve of Li_4-*p*-DOBDA with KB and PTFE (6:3:1), (left) and SP and PTFE (6:3:1), (right); both hand-ground

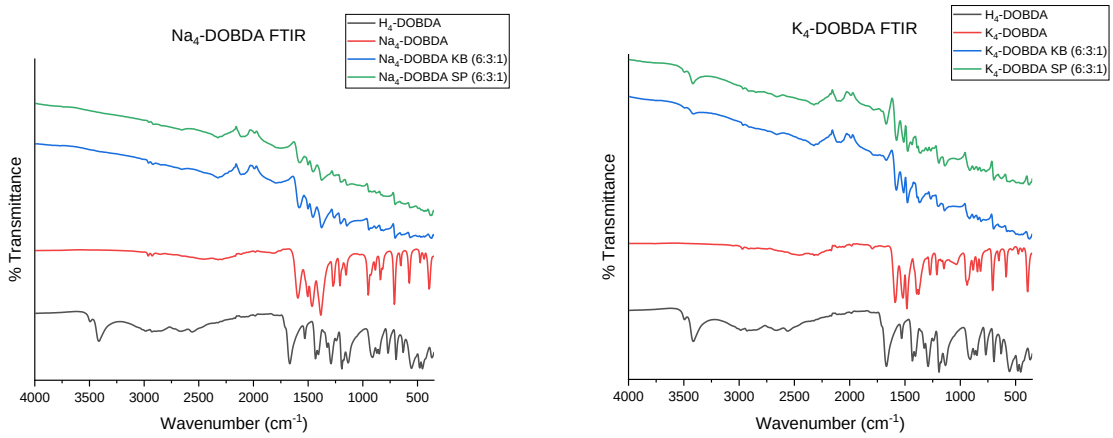

Fig. A7 FTIR graph of Na_4-DOBDA (left) and K_4-DOBDA in comparison with its composites.

Graphene Properties [86]:

Parameter	Value
Electronic mobility	$\sim 2 \times 10^5$ cm^2 V^{-1} s^{-1}
Current density	$\sim 10^9$ A cm^{-1}
Velocity of fermion (electron)	$\sim 10^6$ m s^{-1}
Thermal conductivity	$\sim$5000 W m^{-1} K^{-1}
Tensile strength	$\sim$1.5 Tpa
Breaking strength	42 N m^{-1}
Transparency	$\sim$97.7%
Elastic limit	$\sim$20%
Surface area	$\sim$2360 m^2 g^{-1}

Fig. A8 The Graphene used in the experiment and Properties of Graphene

Fig. A9 Observed Colour change during Synthesis using Schlenk Tube Method (left, after long stirring duration) and Ambient Air Synthesis (right after mixing and gets stirred)

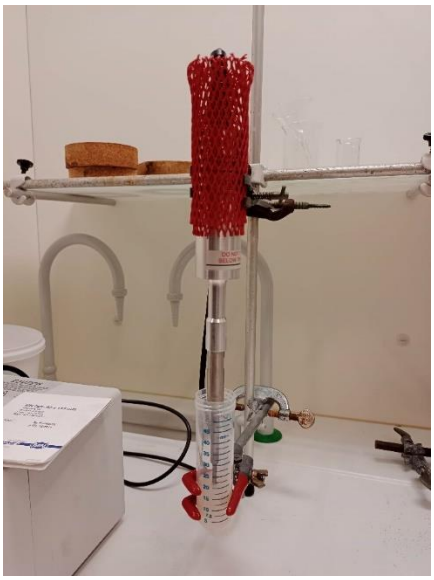

Fig. A10 Probe Sonicator

Fig. A11 Ar-atmosphere Glovebox

Fig. A12 Buchi vacuum dryer

Fig. A13 FTIR (left) and XRD (right) Instruments

Fig. A14 Neware Battery System Tester

VIII. Bibliography

[1] "World Population," 2022. https://www.worldometers.info/world-population/ (accessed: Apr 1st, 2023).

[2] *IEA. Key World Energy Statistics*. 2018. 10.1787/key_energ_stat-2018-en (accessed: Apr 1st, 2023)

[3] C. European Commission. Joint Research, *Li-ion batteries for mobility and stationary storage applications: scenarios for costs and market growth*. LU: Publications Office (in eng), 2018.

[4] "2050 long-term strategy," https://climate.ec.europa.eu/eu-action/climate-strategies-targets/2050-long-term-strategy_en. (accessed: Apr 1st, 2023)

[5] "Sweden, Finland, Latvia: Which EU countries use the most renewable energy?," https://www.euronews.com/green/2023/01/20/which-european-countries-use-the-most-renewable-energy. (accessed: Apr 1st, 2023)

[6] "Wind and water provide most renewable electricity." [Online]. Available: https://ec.europa.eu/eurostat/web/products-eurostat-news/-/ddn-20200129-1.

[7] S. F. Hoefler *et al.*, "New Solar Cell–Battery Hybrid Energy System: Integrating Organic Photovoltaics with Li-Ion and Na-Ion Technologies," *ACS Sustainable Chem. Eng.,* vol. 8, no. 51, pp. 19155-19168, 2020/12/28/ 2020, doi: 10.1021/acssuschemeng.0c0798410.1021/acssuschemeng.0c07984</p>.

[8] "EU ban on the sale of new petrol and diesel cars from 2035 explained," ed. (accessed: Apr 1st, 2023)

[9] "On the electricity excited by the mere contact of conducting substances of different kinds. In a letter from Mr. Alexander Volta, F. R. S. Professor of Natural Philosophy in the University of Pavia, to the Rt. Hon. Sir Joseph Banks, Bart. K. B. P. R. S," (in en), *Proc. R. Soc. Lond.,* vol. 1, pp. 27-29, 1832/12/31/ 1832, doi: 10.1098/rspl.1800.0016.

[10] T. R. Crompton, *Battery reference book*, 3rd ed ed. Oxford, England: Newnes (in eng), 2000.

[11] J.-K. Park, Ed. *Principles and applications of lithium secondary batteries*. Weinheim, Germany: Wiley-VCH, 2012, p. 366.

[12] G. E. Blomgren, "The Development and Future of Lithium Ion Batteries," (in en), *J. Electrochem. Soc.,* vol. 164, no. 1, pp. A5019-A5025, 2017 2017, doi: 10.1149/2.0251701jes.

[13] C.-X. Zu and H. Li, "Thermodynamic analysis on energy densities of batteries," (in en), *Energy Environ. Sci.,* vol. 4, no. 8, p. 2614, 2011 2011, doi: 10.1039/c0ee00777c.

[14] J. M. Tarascon and M. Armand, "Issues and challenges facing rechargeable lithium batteries," (in en), *Nature,* vol. 414, no. 6861, pp. 359-367, 2001/11// 2001, doi: 10.1038/35104644.

[15] M. M. Thackeray, C. Wolverton, and E. D. Isaacs, "Electrical energy storage for transportation—approaching the limits of, and going beyond, lithium-ion batteries," (in en), *Energy Environ. Sci.,* vol. 5, no. 7, p. 7854, 2012 2012, doi: 10.1039/c2ee21892e.

[16] J. Xie and Y.-C. Lu, "A retrospective on lithium-ion batteries," (in en), *Nat Commun,* vol. 11, no. 1, p. 2499, 2020/05/19/ 2020, doi: 10.1038/s41467-020-16259-9.

[17] T.-F. Yi, J. Mei, and Y.-R. Zhu, "Key strategies for enhancing the cycling stability and rate capacity of LiNi0.5Mn1.5O4 as high-voltage cathode materials for high power lithium-ion batteries," (in en), *Journal of Power Sources,* vol. 316, pp. 85-105, 2016/06// 2016, doi: 10.1016/j.jpowsour.2016.03.070.

[18] D. Lin, Y. Liu, and Y. Cui, "Reviving the lithium metal anode for high-energy batteries," (in en), *Nature Nanotech,* vol. 12, no. 3, pp. 194-206, 2017/03// 2017, doi: 10.1038/nnano.2017.16.

[19] K. Deuchert and S. Hünig, "Multistage Organic Redox Systems—A General Structural Principle," (in en), *Angew. Chem. Int. Ed. Engl.,* vol. 17, no. 12, pp. 875-886, 1978/12// 1978, doi: 10.1002/anie.197808753.

[20] J. Li *et al.*, "Toward Low-Cost, High-Energy Density, and High-Power Density Lithium-Ion Batteries," (in en), *JOM,* vol. 69, no. 9, pp. 1484-1496, 2017/09// 2017, doi: 10.1007/s11837-017-2404-9.

[21] J. Heiska, M. Nisula, and M. Karppinen, "Organic electrode materials with solid-state battery technology," (in en), *J. Mater. Chem. A,* vol. 7, no. 32, pp. 18735-18758, 2019 2019, doi: 10.1039/C9TA04328D.

[22] "Samsung's Recall: The Problem With Lithium-Ion Batteries," https://www.nytimes.com/2016/09/03/technology/samsungs-recall-the-problem-with-lithium-ion-batteries.html (accessed: Apr 1st, 2023)

[23] B. Advanced, G. L. I. T. C. G. C. Materials Engineering Research Center, and Q.-f. Zhao, "Recent Advances in LiFePO4 Cathode Materials for Lithium-Ion Batteries. First-Principles Research," *Int. J. Electrochem. Sci.,* p. ArticleID:211226, 2021/12// 2021, doi: 10.20964/2021.12.11.

[24] "2050 long-term strategy." https://climate.ec.europa.eu/eu-action/climate-strategies-targets/2050-long-term-strategy_en (accessed: Apr 1st, 2023)

[25] S. Hess, M. Wohlfahrt-Mehrens, and M. Wachtler, "Flammability of Li-Ion Battery Electrolytes: Flash Point and Self-Extinguishing Time Measurements," (in en), *J. Electrochem. Soc.,* vol. 162, no. 2, pp. A3084-A3097, 2015 2015, doi: 10.1149/2.0121502jes.

[26] P. Greim, A. A. Solomon, and C. Breyer, "Assessment of lithium criticality in the global energy transition and addressing policy gaps in transportation," (in en), *Nat Commun,* vol. 11, no. 1, p. 4570, 2020/09/11/ 2020, doi: 10.1038/s41467-020-18402-y.

[27] S. W. D. Gourley, T. Or, and Z. Chen, "Breaking Free from Cobalt Reliance in Lithium-Ion Batteries," (in en), *iScience,* vol. 23, no. 9, p. 101505, 2020/09// 2020, doi: 10.1016/j.isci.2020.101505.

[28] D. Larcher and J. M. Tarascon, "Towards greener and more sustainable batteries for electrical energy storage," (in en), *Nature Chem,* vol. 7, no. 1, pp. 19-29, 2015/01// 2015, doi: 10.1038/nchem.2085.

[29] C. Delmas, "Sodium and Sodium-Ion Batteries: 50 Years of Research," (in en), *Adv. Energy Mater.,* vol. 8, no. 17, p. 1703137, 2018/06// 2018, doi: 10.1002/aenm.201703137.

[30] C. You *et al.*, "Advances in rechargeable Mg batteries," (in en), *J. Mater. Chem. A,* vol. 8, no. 48, pp. 25601-25625, 2020 2020, doi: 10.1039/D0TA09330K.

[31] J. Kim, Y. Kim, J. Yoo, G. Kwon, Y. Ko, and K. Kang, "Organic batteries for a greener rechargeable world," (in en), *Nat Rev Mater,* vol. 8, no. 1, pp. 54-70, 2022/09/20/ 2022, doi: 10.1038/s41578-022-00478-1.

[32] B. Häupler, A. Wild, and U. S. Schubert, "Carbonyls: Powerful Organic Materials for Secondary Batteries," (in en), *Adv. Energy Mater.,* vol. 5, no. 11, p. 1402034, 2015/06// 2015, doi: 10.1002/aenm.201402034.

[33] K. Oyaizu, T. Kawamoto, T. Suga, and H. Nishide, "Synthesis and Charge Transport Properties of Redox-Active Nitroxide Polyethers with Large Site Density," (in en), *Macromolecules,* vol. 43, no. 24, pp. 10382-10389, 2010/12/28/ 2010, doi: 10.1021/ma1020159.

[34] Y. Lu, Q. Zhang, L. Li, Z. Niu, and J. Chen, "Design Strategies toward Enhancing the Performance of Organic Electrode Materials in Metal-Ion Batteries," (in en), *Chem,* vol. 4, no. 12, pp. 2786-2813, 2018/12// 2018, doi: 10.1016/j.chempr.2018.09.005.

[35] P. Poizot, J. Gaubicher, S. Renault, L. Dubois, Y. Liang, and Y. Yao, "Opportunities and Challenges for Organic Electrodes in Electrochemical Energy Storage," (in en), *Chem. Rev.,* vol. 120, no. 14, pp. 6490-6557, 2020/07/22/ 2020, doi: 10.1021/acs.chemrev.9b00482.

[36] D. L. Williams, J. J. Byrne, and J. S. Driscoll, "A High Energy Density Lithium/Dichloroisocyanuric Acid Battery System," (in en), *J. Electrochem. Soc.,* vol. 116, no. 1, p. 2, 1969 1969, doi: 10.1149/1.2411755.

[37] P. Novák, K. Müller, K. S. V. Santhanam, and O. Haas, "Electrochemically Active Polymers for Rechargeable Batteries," (in en), *Chem. Rev.,* vol. 97, no. 1, pp. 207-282, 1997/02/01/ 1997, doi: 10.1021/cr941181o.

[38] L. Zhan *et al.*, "PEDOT: Cathode active material with high specific capacity in novel electrolyte system," (in en), *Electrochimica Acta,* vol. 53, no. 28, pp. 8319-8323, 2008/11// 2008, doi: 10.1016/j.electacta.2008.06.053.

[39] K. Nakahara *et al.*, "Rechargeable batteries with organic radical cathodes," (in en), *Chemical Physics Letters,* vol. 359, no. 5-6, pp. 351-354, 2002/06// 2002, doi: 10.1016/S0009-2614(02)00705-4.

[40] H. Chen *et al.*, "Lithium Salt of Tetrahydroxybenzoquinone: Toward the Development of a Sustainable Li-Ion Battery," (in en), *J. Am. Chem. Soc.,* vol. 131, no. 25, pp. 8984-8988, 2009/07/01/ 2009, doi: 10.1021/ja9024897.

[41] T. B. Schon, B. T. McAllister, P.-F. Li, and D. S. Seferos, "The rise of organic electrode materials for energy storage," (in en), *Chem. Soc. Rev.,* vol. 45, no. 22, pp. 6345-6404, 2016 2016, doi: 10.1039/C6CS00173D.

[42] P. Colombo, G. Mera, R. Riedel, and G. D. Sorarù, "Polymer-Derived Ceramics: 40 Years of Research and Innovation in Advanced Ceramics: Polymer-Derived Ceramics," (in en), *Journal of the American Ceramic Society,* pp. no-no, 2010/06/07/ 2010, doi: 10.1111/j.1551-2916.2010.03876.x.

[43] L. Zhao *et al.*, "Engineering of sodium-ion batteries: Opportunities and challenges," (in en), *Engineering,* p. S2095809922003630, 2022/05// 2022, doi: 10.1016/j.eng.2021.08.032.

[44] G. G. Eshetu *et al.*, "Electrolytes and Interphases in Sodium-Based Rechargeable Batteries: Recent Advances and Perspectives," (in en), *Adv. Energy Mater.,* vol. 10, no. 20, p. 2000093, 2020/05// 2020, doi: 10.1002/aenm.202000093.

[45] C. O. Laoire, S. Mukerjee, K. M. Abraham, E. J. Plichta, and M. A. Hendrickson, "Influence of Nonaqueous Solvents on the Electrochemistry of Oxygen in the Rechargeable Lithium−Air Battery," (in en), *J. Phys. Chem. C,* vol. 114, no. 19, pp. 9178-9186, 2010/05/20/ 2010, doi: 10.1021/jp102019y.

[46] X. Zhang, A. Wang, X. Liu, and J. Luo, "Dendrites in Lithium Metal Anodes: Suppression, Regulation, and Elimination," *Acc Chem Res,* vol. 52, no. 11, pp. 3223-3232, Nov 19 2019, doi: 10.1021/acs.accounts.9b00437.

[47] J. Conradie, "A Frontier orbital energy approach to redox potentials," *J. Phys.: Conf. Ser.,* vol. 633, p. 012045, 2015/09/21/ 2015, doi: 10.1088/1742-6596/633/1/012045.

[48] H. Shirakawa, E. J. Louis, A. G. MacDiarmid, C. K. Chiang, and A. J. Heeger, "Synthesis of electrically conducting organic polymers: halogen derivatives of polyacetylene, (CH) x," (in en), *J. Chem. Soc., Chem. Commun.,* no. 16, p. 578, 1977 1977, doi: 10.1039/c39770000578.

[49] H. Nishide, S. Iwasa, Y.-J. Pu, T. Suga, K. Nakahara, and M. Satoh, "Organic radical battery: nitroxide polymers as a cathode-active material," (in en), *Electrochimica Acta,* vol. 50, no. 2-3, pp. 827-831, 2004/11// 2004, doi: 10.1016/j.electacta.2004.02.052.

[50] Z. Song and H. Zhou, "Towards sustainable and versatile energy storage devices: an overview of organic electrode materials," (in en), *Energy Environ. Sci.,* vol. 6, no. 8, p. 2280, 2013 2013, doi: 10.1039/c3ee40709h.

[51] K. Oyaizu, T. Suga, K. Yoshimura, and H. Nishide, "Synthesis and Characterization of Radical-Bearing Polyethers as an Electrode-Active Material for Organic Secondary Batteries," (in en), *Macromolecules,* vol. 41, no. 18, pp. 6646-6652, 2008/09/23/ 2008, doi: 10.1021/ma702576z.

[52] B. Häupler *et al.*, "Poly(exTTF): A Novel Redox-Active Polymer as Active Material for Li-Organic Batteries," (in en), *Macromol. Rapid Commun.,* vol. 35, no. 15, pp. 1367-1371, 2014/08// 2014, doi: 10.1002/marc.201400167.

[53] É. Deunf, P. Moreau, É. Quarez, D. Guyomard, F. Dolhem, and P. Poizot, "Reversible anion intercalation in a layered aromatic amine: a high-voltage host structure for organic batteries," (in en), *J. Mater. Chem. A,* vol. 4, no. 16, pp. 6131-6139, 2016 2016, doi: 10.1039/C6TA02356H.

[54] J. Wang *et al.*, "Conjugated sulfonamides as a class of organic lithium-ion positive electrodes," (in en), *Nat. Mater.,* vol. 20, no. 5, pp. 665-673, 2021/05// 2021, doi: 10.1038/s41563-020-00869-1.

[55] X. Liu and Z. Ye, "Nitroaromatics as High-Energy Organic Cathode Materials for Rechargeable Alkali-Ion (Li+, Na+, and K+) Batteries," *Adv. Energy Mater.,* vol. 11, no. 4, 2020, doi: 10.1002/aenm.202003281.

[56] J. Wang *et al.*, "Revealing the reversible solid-state electrochemistry of lithium-containing conjugated oximates for organic batteries," *Sci Adv,* vol. 9, no. 17, p. eadg6079, Apr 28 2023, doi: 10.1126/sciadv.adg6079.

[57] Y. Zhang *et al.*, "Validating the reversible redox of alkali-ion disulfonyl-methanide as organic positive electrode materials," *Materials Today Chemistry,* vol. 28, 2023, doi: 10.1016/j.mtchem.2023.101379.

[58] H.-C. Kuan *et al.*, "A nitrogen- and carbonyl-rich conjugated small-molecule organic cathode for high-performance sodium-ion batteries," *J. Mater. Chem. A,* vol. 10, no. 30, pp. 16249-16257, 2022, doi: 10.1039/d2ta03953b.

[59] M. Armand *et al.*, "Conjugated dicarboxylate anodes for Li-ion batteries," *Nat Mater,* vol. 8, no. 2, pp. 120-5, Feb 2009, doi: 10.1038/nmat2372.

[60] M. López-Herraiz, E. Castillo-Martínez, J. Carretero-González, J. Carrasco, T. Rojo, and M. Armand, "Oligomeric-Schiff bases as negative electrodes for sodium ion batteries: unveiling the nature of their active redox centers," *Energy Environ. Sci.,* vol. 8, no. 11, pp. 3233-3241, 2015, doi: 10.1039/c5ee01832c.

[61] C. Luo *et al.*, "Azo compounds as a family of organic electrode materials for alkali-ion batteries," *Proc Natl Acad Sci U S A,* vol. 115, no. 9, pp. 2004-2009, Feb 27 2018, doi: 10.1073/pnas.1717892115.

[62] A. E. Lakraychi, F. Dolhem, A. Vlad, and M. Becuwe, "Organic Negative Electrode Materials for Metal-Ion and Molecular-Ion Batteries: Progress and Challenges from a Molecular Engineering Perspective," *Adv. Energy Mater.,* vol. 11, no. 32, 2021, doi: 10.1002/aenm.202101562.

[63] B. Esser, F. Dolhem, M. Becuwe, P. Poizot, A. Vlad, and D. Brandell, "A perspective on organic electrode materials and technologies for next generation batteries," *Journal of Power Sources,* vol. 482, 2021, doi: 10.1016/j.jpowsour.2020.228814.

[64] L. Sieuw *et al.*, "Through-Space Charge Modulation Overriding Substituent Effect: Rise of the Redox Potential at 3.35 V in a Lithium-Phenolate Stereoelectronic Isomer," (in en), *Chem. Mater.,* vol. 32, no. 23, pp. 9996-10006, 2020/12/08/ 2020, doi: 10.1021/acs.chemmater.0c02989.

[65] M. Liu and S. Lu, "Plastoquinone and Ubiquinone in Plants: Biosynthesis, Physiological Function and Metabolic Engineering," *Front. Plant Sci.,* vol. 7, 2016/12/16/ 2016, doi: 10.3389/fpls.2016.01898.

[66] M. Quan, D. Sanchez, M. F. Wasylkiw, and D. K. Smith, "Voltammetry of Quinones in Unbuffered Aqueous Solution: Reassessing the Roles of Proton Transfer and Hydrogen Bonding in the Aqueous Electrochemistry of Quinones," (in en), *J. Am. Chem. Soc.,* vol. 129, no. 42, pp. 12847-12856, 2007/10/01/ 2007, doi: 10.1021/ja0743083.

[67] Q. Zhao, C. Guo, Y. Lu, L. Liu, J. Liang, and J. Chen, "Rechargeable Lithium Batteries with Electrodes of Small Organic Carbonyl Salts and Advanced Electrolytes," (in en), *Ind. Eng. Chem. Res.,* vol. 55, no. 20, pp. 5795-5804, 2016/05/25/ 2016, doi: 10.1021/acs.iecr.6b01462.

[68] S. i. Tobishima, J. i. Yamaki, and A. Yamaji, "Cathode Characteristics of Organic Electron Acceptors for Lithium Batteries," *J. Electrochem. Soc.,* vol. 131, no. 1, pp. 57-63, 1984/01/01/ 1984, doi: 10.1149/1.2115542.

[69] Y. Lu *et al.*, "Cyclohexanehexone with Ultrahigh Capacity as Cathode Materials for Lithium-Ion Batteries," (in en), *Angew. Chem. Int. Ed.,* vol. 58, no. 21, pp. 7020-7024, 2019/05/20/ 2019, doi: 10.1002/anie.201902185.

[70] A. E. Lakraychi *et al.*, "An air-stable lithiated cathode material based on a 1,4-benzenedisulfonate backbone for organic Li-ion batteries," (in en), *J. Mater. Chem. A,* vol. 6, no. 39, pp. 19182-19189, 2018 2018, doi: 10.1039/C8TA07097K.

[71] L. Sieuw *et al.*, "A H-bond stabilized quinone electrode material for Li–organic batteries: the strength of weak bonds," (in en), *Chem. Sci.,* vol. 10, no. 2, pp. 418-426, 2019 2019, doi: 10.1039/C8SC02995D.

[72] S. Gottis, A.-L. Barrès, F. Dolhem, and P. Poizot, "Voltage Gain in Lithiated Enolate-Based Organic Cathode Materials by Isomeric Effect," (in en), *ACS Appl. Mater. Interfaces,* vol. 6, no. 14, pp. 10870-10876, 2014/07/23/ 2014, doi: 10.1021/am405470p.

[73] A. E. Lakraychi, S. De Kreijger, D. Gupta, B. Elias, and A. Vlad, "Phendione–Transition-Metal Complexes with Bipolar Redox Activity for Lithium Batteries," (in en), *ChemSusChem,* vol. 13, no. 9, pp. 2225-2231, 2020/05/08/ 2020, doi: 10.1002/cssc.201903290.

[74] P. Poizot and F. Dolhem, "Clean energy new deal for a sustainable world: from non-CO2 generating energy sources to greener electrochemical storage devices," (in en), *Energy Environ. Sci.,* vol. 4, no. 6, p. 2003, 2011 2011, doi: 10.1039/c0ee00731e.

[75] S. Renault *et al.*, "A green Li–organic battery working as a fuel cell in case of emergency," (in en), *Energy Environ. Sci.,* vol. 6, no. 7, p. 2124, 2013 2013, doi: 10.1039/c3ee40878g.

[76] S. Wang, L. Wang, K. Zhang, Z. Zhu, Z. Tao, and J. Chen, "Organic Li ₄ C ₈ H ₂ O ₆ Nanosheets for Lithium-Ion Batteries," (in en), *Nano Lett.,* vol. 13, no. 9, pp. 4404-4409, 2013/09/11/ 2013, doi: 10.1021/nl402239p.

[77] T. Nokami *et al.*, "Polymer-bound pyrene-4,5,9,10-tetraone for fast-charge and -discharge lithium-ion batteries with high capacity," *J Am Chem Soc,* vol. 134, no. 48, pp. 19694-700, Dec 5 2012, doi: 10.1021/ja306663g.

[78] G. Nystrom, A. Razaq, M. Stromme, L. Nyholm, and A. Mihranyan, "Ultrafast all-polymer paper-based batteries," *Nano Lett,* vol. 9, no. 10, pp. 3635-9, Oct 2009, doi: 10.1021/nl901852h.

[79] J. Chen and F. Cheng, "Combination of lightweight elements and nanostructured materials for batteries," *Acc Chem Res,* vol. 42, no. 6, pp. 713-23, Jun 16 2009, doi: 10.1021/ar800229g.

[80] M. Stein *et al.*, "Probing the Effect of High Energy Ball Milling on the Structure and Properties of LiNi1/3Mn1/3Co1/3O2 Cathodes for Li-Ion Batteries," *Journal of Electrochemical Energy Conversion and Storage,* vol. 13, no. 3, 2016, doi: 10.1115/1.4034755.

[81] "Graphene Synthesis, Properties, And Applications." [Online]. Available: https://www.cheaptubes.com/graphene-synthesis-properties-and-applications/. (accessed: Apr 1st, 2023)

[82] "Bragg's Law." https://chem.libretexts.org/Bookshelves/Analytical_Chemistry/Supplemental_Modules_(Analytical_Chemistry)/Instrumentation_and_Analysis/Diffraction_Scattering_Techniques/Bragg's_Law (accessed: Apr 1st, 2023)

[83] A. L. Patterson, "The Scherrer Formula for X-Ray Particle Size Determination," *Physical Review,* vol. 56, no. 10, pp. 978-982, 1939, doi: 10.1103/PhysRev.56.978.

[84] J. Zmpitas and J. Gross, "Modified Stokes–Einstein Equation for Molecular Self-Diffusion Based on Entropy Scaling," *Ind. Eng. Chem. Res.,* vol. 60, no. 11, pp. 4453-4459, 2021, doi: 10.1021/acs.iecr.0c06090.

[85] S. A. Rice, "On the Bjerrum Relation and the Formation of Ion Pairs," *J. Am. Chem. Soc.,* vol. 78, no. 20, pp. 5247-5252, 2002, doi: 10.1021/ja01601a028.

[86] S. Dash and A. Patnaik, "Material selection for THz antennas," *Microwave and Optical Technology Letters,* vol. 60, no. 5, pp. 1183-1187, 2018, doi: 10.1002/mop.31127.

UNIVERSITÉ CATHOLIQUE DE LOUVAIN
École polytechnique de Louvain
Rue Archimède, 1 bte L6.11.01, 1348 Louvain-la-Neuve, Belgique | **www.uclouvain.be/epl**